From weakly to strongly nonlinear viscous drop shape oscillations: An analytical and numerical study

Martin Smuda ◉, Florian Kummer ◉, and Martin Oberlack ◉
Chair of Fluid Dynamics, TU Darmstadt, Otto-Berndt-Straße 2, D-64287 Darmstadt, Germany

Dino Zrnić ◉ and Günter Brenn ◉*
Institute of Fluid Mechanics and Heat Transfer, Graz University of Technology, A-8010 Graz, Austria

Nonlinear axisymmetric shape oscillations of a Newtonian drop in a vacuum are investigated using two different theoretical methods, for fundamental interest and for the significance of the oscillations in transport processes across the drop surface. The extended discontinuous Galerkin method is contrasted to the weakly nonlinear theory. While the former allows large drop surface deformation amplitudes to be analyzed with high precision and drop volume errors below 0.11% even at the largest deformations, the latter provides analytical insight into the origin of quasiperiodic time behavior of the oscillations and reveals the oscillation modes coupled in the nonlinear motion. Results from both methods for moderate initial deformation amplitudes at modes of initial drop deformation $m = 2$, 3, and 4 are in excellent agreement, showing the time asymmetry of the oscillation and the decrease of the oscillation frequency with increasing deformation amplitude. The Fourier power spectra for the first oscillation period exhibit decreased dominant frequencies as compared to the linear results as well as the mode coupling as nonlinear effects. The numerical method is used to compute the oscillatory and damping behavior of viscous drops, as well as the interconversion of kinetic and surface energies during the oscillations at strong initial deformations.

I. INTRODUCTION

Shape oscillations of individual drops have been investigated in science for more than a century. The shape oscillations influence transport processes due to the increase of the drop surface area caused by the deformations, and due to fluid motion induced by the oscillations in both the drop and the host medium. Furthermore, linear drop shape oscillations are established as a means for measuring capillary and rheological properties of the drop liquid. A detailed review of the literature on the subject, starting from Rayleigh's work [1], can be found in our earlier papers [2,3]. We do not wish to repeat this here.

Research on nonlinear drop shape oscillations with large amplitudes using computational methods started from the work of Foote [4] and Alonso [5]. The latter author carried her simulations to a point where the deformations may lead to fission of the drop. Experiments on large-amplitude drop

---

*Contact author: guenter.brenn@tugraz.at

shape oscillations are attributed to Marston and Apfel [6,7]. Neutrally buoyant, immiscible drops were acoustically excited to quadrupole shape oscillations, carrying the deformations to a degree that the drops split into two or more fragments. The authors proposed this technique as a candidate for emulsification.

Thereafter, Trinh and Wang carried out experiments on large-amplitude drop shape oscillations with a similar technique [8]. The drops were neutrally buoyant in an immiscible host liquid and positioned by a standing pressure wave produced by ultrasound. Modulation of the ultrasound excited the shape oscillations. In the analysis of the acoustically excited drop shape oscillations, the influence of the immiscible host liquid was taken into account. Interest was focused on the damping factor of the oscillations.

In his paper [9], Basaran presented numerical simulations of nonlinear shape oscillations of viscous drops. His results showed the influence from mode coupling on the oscillations, revealing a quasiperiodic oscillation dynamic. Experiments on the breakup of oscillating, electrically charged drops were conducted by Basaran *et al.* [10]. The focus of the study was on the effects of the electric field on the stability of the drops. The oscillation frequency of conducting inviscid drops was reported to decrease quadratically with increasing electric field strength. Electrically induced breakup occurs with tiny jets formed on the drop surface, which break up into small droplets, as applied in electrospraying.

The special cases of drops, which are initially deformed due to pinch-off from a tube end, and of other initially nonspherical drops falling in air were investigated in Refs. [11–14]. Reference [11] studies the pinch-off and the falling motion of an individual water drop in air, revealing both the translational motion and the shape oscillations of the drop. The interaction between the shape oscillations and the translational motion of the drop induces complex dynamics. Nonlinear effects on the shape oscillations due to the initial drop shape and velocity field in the drop are found. In Refs. [12–14], nonspherical oscillating drops falling in air are studied both experimentally and numerically. The drop surface shapes evolve in time, starting from initial values of their axis length ratios. Oscillation frequencies differ from the Rayleigh value by no more than 8%. An influence on the shape oscillations from the orientation of the drop symmetry axes relative to the falling direction is seen.

The scientific importance of oscillating drops extends to their use for measuring physical properties of the drop liquid. Material properties measured are the dynamic viscosity [15,16], the liquid surface tension against the ambient gas [17], and the interfacial tension between immiscible liquids [18]. For drops from complex fluids, rheological properties of the drop surface were measured in Refs. [19–21], also for large drop deformations. A growing-drop technique was used by Zhang *et al.* for measuring the dynamic surface tension of the drop liquid in contact with an ambient gas [22]. However, shape oscillations of the pendant drop prevent the measurements in the first 20 ms after formation of the interface. The breakup of surfactant-laden drops was studied in Ref. [23]. The authors deduced the surfactant content from shape oscillations of satellite droplets. Nonlinear drop shape oscillations, with a particular view on the damping rate, are of key importance for all these measurements, and detailed understanding is crucial for the application. A comprehensive review of measuring techniques based on oscillating drops and bubbles is attributed to Kovalchuk *et al.* [24].

The present paper studies the oscillation and damping behaviors of individual drops at large deformation amplitudes, a subject that is not sufficiently studied theoretically in the literature. The work is structured as follows: In the next section, the problem of viscous drop shape oscillations is stated by the governing equations with their initial and boundary conditions. Section III introduces the weakly nonlinear analysis, together with the emerging balance equations, up to the second order of approximation. For the sake of readability of the text, for the third-order approximation and the solutions of the various approximation orders, the reader is referred to our earlier paper [3]. Section IV gives an introduction to the extended discontinuous Galerkin method used for the present problem within a two-phase formulation. Section V presents results on the oscillating drop, comparing the numerical simulations to results from the weakly nonlinear theory and analyzing large-amplitude oscillations. The paper ends with the conclusions in Sec. VI.
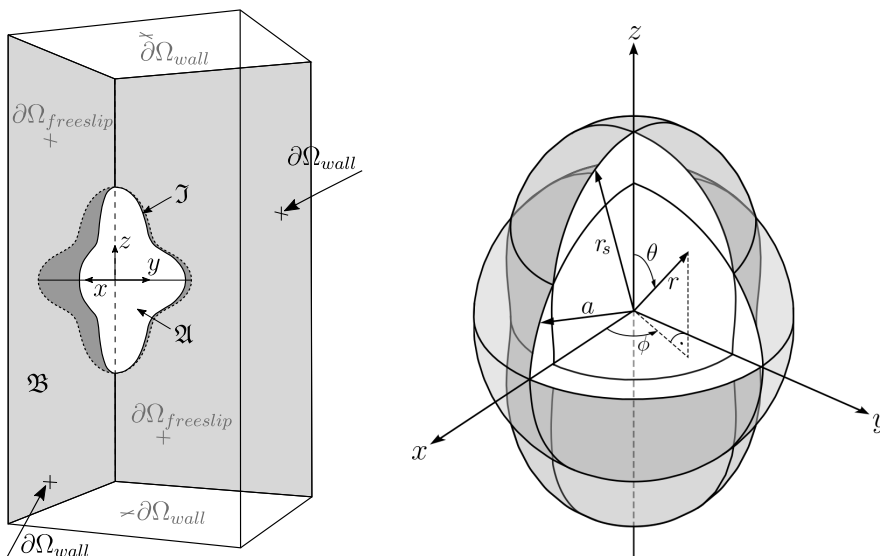
FIG. 1. Domain definitions for the investigation of deformed viscous droplets. Left: Computational domain Ω for a two-phase setting with the interface $\mathfrak{I}$ separating the droplet $\mathfrak{A}$ from the ambient phase $\mathfrak{B}$. The boundary is a disjoint decomposition into wall $\partial\Omega_{wall}$ and free slip regions $\partial\Omega_{freeslip}$ (grey areas). Right: Droplet representation in spherical coordinates (r, θ, ϕ). Spherical droplet at rest with radius a and deformed droplet with local droplet radius $r_s = r_s(\theta, \phi)$,

II. PROBLEM STATEMENT

Shape oscillations of an axisymmetric viscous liquid drop are studied analytically, using the weakly nonlinear theory (WNLT) [2,3], and numerically, using the extended discontinuous Galerkin (XDG) method. The liquid is incompressible and Newtonian, and body forces are not accounted for. The equations of motion, together with the boundary and initial conditions, are nondimensionalized with the undeformed drop radius a, the capillary timescale $(\rho a^3/\sigma)^{1/2}$, and the capillary pressure σ/a for length, time, and pressure, respectively. The resulting dimensionless transient incompressible Navier-Stokes equations read

$$\nabla \cdot \boldsymbol{u} = 0 \quad \text{in} \quad \Omega \setminus \mathfrak{I}, \tag{1a}$$

$$\frac{\partial \boldsymbol{u}}{\partial t} + \nabla \cdot (\boldsymbol{u} \otimes \boldsymbol{u}) = \nabla \cdot [-p\boldsymbol{I} + Oh(\nabla \boldsymbol{u} + (\nabla \boldsymbol{u})^\top)] \quad \text{in} \quad \Omega \setminus \mathfrak{I}, \tag{1b}$$

where the Ohnesorge number $Oh = \mu/(\sigma a \rho)^{1/2}$ (with the liquid dynamic viscosity μ, surface tension σ, and density ρ) measures the capillary against the viscous timescale. For the numerical simulation with XDG, we consider the two-phase setting within a sharp-interface formulation and restrict the domain to a quarter of the droplet (see Fig. 1, left). We define the computational domain $\Omega \subset \mathbb{R}^3$ as the disjoint partitioning of the time-dependent fluid bulk phases $\mathfrak{A}(t)$ (droplet phase) and $\mathfrak{B}(t)$ (ambient phase) and the moving interface $\mathfrak{I}(t)$ by

$$\Omega = \mathfrak{A}(t) \,\dot{\cup}\, \mathfrak{I}(t) \,\dot{\cup}\, \mathfrak{B}(t). \tag{2}$$

The drop surface $\mathfrak{I}(t)$ is defined as the position with the radial distance $r_s(\theta, t) = 1 + \eta(\theta, t)$ from the origin of the coordinate system (see Fig. 1, right). The distance η is the deformation against the spherical shape with normalized radius 1.

A. Boundary conditions

Within the two-phase setting for the XDG method, the boundary conditions at the computational domain boundary $\partial\Omega = \partial\Omega_{\text{wall}} \,\dot{\cup}\, \partial\Omega_{\text{freeslip}}$, describing a disjoint decomposition into wall, $\partial\Omega_{\text{wall}}$, and free slip regions, $\partial\Omega_{\text{freeslip}}$ (grey areas in Fig. 1, left), read

$$\boldsymbol{u} = \boldsymbol{0} \quad \text{on} \quad \partial\Omega_{\text{wall}}, \tag{3a}$$

$$\boldsymbol{u} \cdot \boldsymbol{n}_{\partial\Omega} = 0 \quad \text{and} \quad \boldsymbol{\tau}_{\partial\Omega} \cdot (\nabla\boldsymbol{u} + (\nabla\boldsymbol{u})^{\top}) \cdot \boldsymbol{n}_{\partial\Omega} = 0 \quad \text{on} \quad \partial\Omega_{\text{freeslip}}, \tag{3b}$$

where $\boldsymbol{n}_{\partial\Omega}$ and $\boldsymbol{\tau}_{\partial\Omega}$ describe the normal and tangential vectors on the boundary $\partial\Omega$. Note that there is only negligible influence of boundary condition (3a) on the results shown below. Indeed, exemplary calculations were also performed with a free-flow boundary condition instead of wall boundary condition and no significant difference in the results could be observed.

At the material interface $\mathfrak{I}$, located within the computational domain Ω, the corresponding jump conditions for the Navier-Stokes equations (1) are given by

$$[\![\boldsymbol{u}]\!] = \boldsymbol{0} \quad \text{on} \quad \mathfrak{I}, \tag{4a}$$

$$[\![-p\boldsymbol{n}_{\mathfrak{I}} + Oh(\nabla\boldsymbol{u} + (\nabla\boldsymbol{u})^{\top}) \cdot \boldsymbol{n}_{\mathfrak{I}}]\!] = \kappa\boldsymbol{n}_{\mathfrak{I}} \quad \text{on} \quad \mathfrak{I}, \tag{4b}$$

where the jump operator $[\![\cdot]\!]$ is defined as $[\![f]\!] := (\lim_{\xi\searrow 0} f(\boldsymbol{x} - \xi\boldsymbol{n}_{\mathfrak{I}}) - \lim_{\xi\searrow 0} f(\boldsymbol{x} + \xi\boldsymbol{n}_{\mathfrak{I}}))$ for $\boldsymbol{x} \in \mathfrak{I}$. In the momentum jump condition (4b) on the right-hand side, $\kappa = (\nabla \cdot \boldsymbol{n}_{\mathfrak{I}})$ denotes the dimensionless mean curvature of the interface $\mathfrak{I}$. The outward interface normal $\boldsymbol{n}_{\mathfrak{I}}$ pointing from $\mathfrak{A}$ to $\mathfrak{B}$ is computed from the level-set function $\varphi(\theta, t) = r - r_s(\theta, t)$ via

$$\boldsymbol{n}_{\mathfrak{I}} = \frac{\nabla\varphi}{|\nabla\varphi|}. \tag{5}$$

With the WNLT, the following single-phase boundary conditions at the interface $\mathfrak{I}$ are used: the kinematic boundary condition, stating that the material rate of deformation of the drop surface equals the radial velocity component at the place of the deformed surface, i.e.,

$$u_r = \frac{D\eta}{Dt} = \frac{\partial\eta}{\partial t} + \frac{u_{\theta}}{r}\frac{\partial\eta}{\partial\theta} \quad \text{at} \quad r = r_s, \tag{6}$$

the dynamic boundary condition, stating that the shear stress at the drop surface is zero and reads

$$(\boldsymbol{n}_{\mathfrak{I}} \cdot (\nabla\boldsymbol{u} + (\nabla\boldsymbol{u})^{\top})) \times \boldsymbol{n}_{\mathfrak{I}} = \boldsymbol{0} \quad \text{at} \quad r = r_s, \tag{7}$$

and the dynamic boundary condition, stating that the normal stress at the drop surface, which is composed of the static pressure, the viscous normal stress, and the capillary stress, is zero, i.e.,

$$-p + Oh(\boldsymbol{n}_{\mathfrak{I}} \cdot (\nabla\boldsymbol{u} + (\nabla\boldsymbol{u})^{\top})) \cdot \boldsymbol{n}_{\mathfrak{I}} + (\nabla \cdot \boldsymbol{n}_{\mathfrak{I}}) = 0 \quad \text{at} \quad r = r_s. \tag{8}$$

B. Initial conditions

In order to close the initial-boundary-value problem for the XDG method, we set an initial condition for the velocity field by

$$\boldsymbol{u}(\boldsymbol{x}, 0) = \boldsymbol{u}_0(\boldsymbol{x}) \quad \text{with} \quad \nabla \cdot \boldsymbol{u}_0 = 0 \quad \text{for} \quad \boldsymbol{x} \in \Omega \setminus \mathfrak{I}(0), \tag{9}$$

where the initial interface position $\mathfrak{I}(0)$ is given. The material interface evolves according to the bulk velocity $\boldsymbol{u}(\boldsymbol{x}, t)$ at $\boldsymbol{x} \in \mathfrak{I}(t)$.

With the WNLT, a first initial condition describes the initial shape of the drop surface r_0 by a Legendre polynomial $P_m(\cos\theta)$ of degree m with the deformation parameter η_0, in a general form written as

$$r_0(\theta) = r_s(\theta, 0) = A(\theta) + \eta_0 P_m(\cos\theta). \tag{10}$$

For the undeformed state, i.e., when $\eta_0 = 0$, we have $A(\theta) = 1$. The second initial condition states that the drop surface initially does not move in the radial direction; i.e., it reads

$$\left.\frac{\partial r_s(\theta, t)}{\partial t}\right|_{t=0} = 0. \tag{11}$$

The initial conditions relating to the velocity field in the drop are different for the XDG method and the WNLT, since the solutions of the WNLT determine the velocity field at all times, including $t = 0$, while the XDG method leaves the freedom to set an initial velocity field.

III. THE WEAKLY NONLINEAR THEORY

For the weakly nonlinear analysis of the problem, the governing equations (1) are formulated in spherical coordinates in a nondimensional form, as introduced in Sec. II. The equations are solved subject to boundary conditions (6)–(8), and with the initial conditions (10) and (11) in their nondimensional forms [3].

For developing the solutions, the field variables are expanded in power series with respect to the small deformation parameter η_0. As an example,

$$u_r(r, \theta, t) = u_{r1}(r, \theta, t)\eta_0 + u_{r2}(r, \theta, t)\eta_0^2 + u_{r3}(r, \theta, t)\eta_0^3 + \cdots, \tag{12}$$

$$p(r, \theta, t) = 2 + p_1(r, \theta, t)\eta_0 + p_2(r, \theta, t)\eta_0^2 + p_3(r, \theta, t)\eta_0^3 + \cdots, \tag{13}$$

$$\eta(\theta, t) = \eta_1(\theta, t)\eta_0 + \eta_2(\theta, t)\eta_0^2 + \eta_3(\theta, t)\eta_0^3 + \cdots. \tag{14}$$

For convergence of these series expansions, the deformation parameter η_0 must be small as compared to unity. An important difference between the linear and the weakly nonlinear analyses is that the boundary conditions are satisfied on the deformed drop surface, not on the undeformed spherical surface. For doing this, but still allowing for the functions in the boundary conditions to be evaluated on the undeformed drop surface, their values on the deformed surface are represented by Taylor expansions, such as, for example for u_r and p,

$$u_r|_{r=1+\eta} = u_r|_{r=1} + \left.\frac{\partial u_r}{\partial r}\right|_{r=1} \eta + \cdots, \tag{15}$$

$$p|_{r=1+\eta} = p|_{r=1} + \left.\frac{\partial p}{\partial r}\right|_{r=1} \eta + \cdots. \tag{16}$$

The initial deformed drop shape, which is governed by a Legendre polynomial of degree m and the amplitude η_0, reads

$$r_s(\theta, 0) = 1 + \eta(\theta, 0) = 1 + \eta_0 P_m(\cos\theta) - \eta_0^2 \frac{1}{2m+1} - \frac{\eta_0^3}{6} \int_{-1}^{1} P_m(\cos\theta)^3 d(\cos\theta) \mp \cdots. \tag{17}$$

Substituting these approaches into the nondimensionalized equations of motion (1) and into boundary conditions (6)–(8), and representing the flow properties and their derivatives as given in Eqs. (12)–(16), we obtain sets of first-, second-, and third-order equations of motion and boundary conditions, consisting of all the terms with the deformation parameter η_0 to the first, second, and third powers, respectively. The same applies to the initial conditions. For details of this method refer to Ref. [3]. To ensure readability and to understand the final results we present certain details.

A. First-order equations

The first-order equations consist of all terms in the equations of motion with the parameter η_0 to the first power. The first-order continuity and momentum equations in vector form read

$$\nabla \cdot \boldsymbol{u}_1 = 0, \tag{18}$$

$$\frac{\partial \boldsymbol{u}_1}{\partial t} - \boldsymbol{\nabla} \cdot (-p_1 \boldsymbol{I} + Oh(\boldsymbol{\nabla} \boldsymbol{u}_1 + (\boldsymbol{\nabla} \boldsymbol{u}_1)^\top)) = 0 \,. \tag{19}$$

The first-order boundary conditions are satisfied at $r = 1$, and we obtain

$$u_{r1} = \frac{\partial \eta_1}{\partial t}, \quad \text{kinematic}, \tag{20}$$

$$r \frac{\partial}{\partial r} \left(\frac{u_{\theta 1}}{r} \right) + \frac{1}{r} \frac{\partial u_{r1}}{\partial \theta} = 0, \quad \text{zero shear stress}, \tag{21}$$

$$-p_1 + 2Oh \frac{\partial u_{r1}}{\partial r} - \left(2\eta_1 + \frac{\partial \eta_1}{\partial \theta} \cot \theta + \frac{\partial^2 \eta_1}{\partial \theta^2} \right) = 0, \quad \text{zero normal stress}. \tag{22}$$

Furthermore, the initial conditions of first order are

$$\eta_1(\theta, 0) = P_m(\cos \theta) \quad \text{and} \quad \frac{\partial \eta_1}{\partial t}(\theta, 0) = 0 \,. \tag{23}$$

The first initial condition determines the initial shape of the deformed drop by a Legendre polynomial $P_m(\cos \theta)$ of order m, and the second condition states that the drop surface initially does not move in the radial direction.

B. Second-order equations

The second-order equations with their boundary and initial conditions are obtained as all the terms from the equations of motion with the parameter η_0 to the second power. The second-order continuity and momentum equations in vector form read

$$\boldsymbol{\nabla} \cdot \boldsymbol{u}_2 = 0 \,, \tag{24}$$

$$\frac{\partial \boldsymbol{u}_2}{\partial t} - \boldsymbol{\nabla} \cdot (-p_2 \boldsymbol{I} + Oh(\boldsymbol{\nabla} \boldsymbol{u}_2 + (\boldsymbol{\nabla} \boldsymbol{u}_2)^\top)) = -\boldsymbol{\nabla} \cdot (\boldsymbol{u}_1 \otimes \boldsymbol{u}_1). \tag{25}$$

The second-order kinematic boundary condition along with the boundary conditions defining zero shear and normal stresses, to be satisfied at $r = 1$, are

$$u_{r2} - \frac{\partial \eta_2}{\partial t} = \frac{u_{\theta 1}}{r} \frac{\partial \eta_1}{\partial \theta} - \eta_1 \frac{\partial u_{r1}}{\partial r}, \tag{26}$$

$$r \frac{\partial}{\partial r} \left(\frac{u_{\theta 2}}{r} \right) + \frac{1}{r} \frac{\partial u_{r2}}{\partial \theta} = -\eta_1 \frac{\partial}{\partial r} \left(r \frac{\partial}{\partial r} \left(\frac{u_{\theta 1}}{r} \right) + \frac{1}{r} \frac{\partial u_{r1}}{\partial \theta} \right)$$
$$- 2 \left(r \frac{\partial}{\partial r} \left(\frac{u_{r1}}{r} \right) - \frac{1}{r} \frac{\partial u_{\theta 1}}{\partial \theta} \right) \frac{1}{r} \frac{\partial \eta_1}{\partial \theta}, \tag{27}$$

$$- p_2 + 2Oh \frac{\partial u_{r2}}{\partial r} - \left(2\eta_2 + \frac{\partial \eta_2}{\partial \theta} \cot \theta + \frac{\partial^2 \eta_2}{\partial \theta^2} \right)$$
$$= \eta_1 \frac{\partial p_1}{\partial r} - \left(2\eta_1^2 + 2\eta_1 \frac{\partial \eta_1}{\partial \theta} \cot \theta + 2\eta_1 \frac{\partial^2 \eta_1}{\partial \theta^2} \right)$$
$$- 2Oh \left[\eta_1 \frac{\partial^2 u_{r1}}{\partial r^2} - \frac{1}{r} \frac{\partial \eta_1}{\partial \theta} \left(r \frac{\partial}{\partial r} \left(\frac{u_{\theta 1}}{r} \right) + \frac{1}{r} \frac{\partial u_{r1}}{\partial \theta} \right) \right], \tag{28}$$

respectively. In addition, the second-order initial conditions are

$$\eta_2(\theta, 0) = -\frac{1}{2m + 1}, \quad \frac{\partial \eta_2}{\partial t}(\theta, 0) = 0. \tag{29}$$

The first initial condition ensures volume conservation, and the second condition states that, initially, the drop surface does not move in the radial direction.

In order maintain readability of the paper, we refer the reader to the details of the solutions of the above derived equations given in Ref. [3] and its supplementary materials, where the solutions are extended to the third order of approximation. Solving the sets of first-, second-, and third-order equations, together with their boundary and initial conditions, reveals as nonlinear effects a frequency change and an excess time the drop spends in an elongated state, both as functions of the initial deformation amplitude. The third order of approximation of the analysis ensures that these effects are represented to a satisfactory degree of accuracy.

IV. THE EXTENDED DISCONTINUOUS GALERKIN METHOD

This section presents the method used for the direct numerical simulations with the XDG method [25], also referred to as the unfitted discontinuous Galerkin (DG) [26] or cut-cell DG method. All the XDG simulations are performed with the XNSE-Solver within the open-source solver framework Bounded Support Spectral Solver (BoSSS) [27] developed at the Chair of Fluid Dynamics of the TU Darmstadt in Germany. The implemented method is based on the work in Ref. [28].

The starting point of the XDG discretization is a standard DG polynomial basis $\Phi = (\Phi_{j,n})_{j=1,\dots,J, n=0,\dots,N_k}$, where J and N_k denote the number of cells and the number of polynomials up to degree k, respectively. The individual functions $\Phi_{j,n}(\boldsymbol{x})$ are defined as polynomials within the computational cell K_j and zero outside. In the XDG approach, the approximation space is adapted in every time step to be conformal with the fluid interface $\mathfrak{I}(t)$. The interface is represented by a level-set function $\varphi(\boldsymbol{x}, t)$, such that

$$\mathfrak{I}(t) = \{\boldsymbol{x} \in \Omega : \varphi(\boldsymbol{x}, t) = 0\}, \quad \mathfrak{A}(t) = \{\boldsymbol{x} \in \Omega : \varphi(\boldsymbol{x}, t) < 0\}, \quad \mathfrak{B}(t) = \{\boldsymbol{x} \in \Omega : \varphi(\boldsymbol{x}, t) > 0\}. \tag{30}$$

The adaption of the approximation space is obtained by multiplying the basis functions $\Phi_{j,n}(\boldsymbol{x})$ with the Heaviside function of φ; i.e., some field quantity $g(\boldsymbol{x}, t)$ is approximated as a weighted sum by

$$g(\boldsymbol{x}, t) = \sum_{j,n} g_{j,n}^{\mathfrak{A}}(t) H(-\varphi(\boldsymbol{x}, t)) \Phi_{j,n}(\boldsymbol{x}) + g_{j,n}^{\mathfrak{B}}(t) H(+\varphi(\boldsymbol{x}, t)) \Phi_{j,n}(\boldsymbol{x}). \tag{31}$$

In each cut cell (a cell intersected by the interface $\mathfrak{I}$) this yields separate degrees of freedom $g_{j,n}^{\mathfrak{A}}(t)$ and $g_{j,n}^{\mathfrak{B}}(t)$ for the liquid domain $\mathfrak{A}$ and ambient domain $\mathfrak{B}$, respectively. Since the XDG basis functions $H(\pm\varphi(\boldsymbol{x}, t))\Phi_{j,n}(\boldsymbol{x})$ are conformal with the interface, the XDG method allows sharp and subcell accurate representation of kinks in the velocity fields as well as discontinuities in the pressure.

For the spatial discretization, the function spaces of the ansatz and test functions for the components of the velocity fields $\boldsymbol{u} \in \mathbb{R}^3$ are discretized by XDG spaces of order k and the pressure field $p \in \mathbb{R}$ of order $k' = k - 1$.

The discretization in time is done with the moving interface approach following the work of Ref. [29], where a BDF3 scheme is used. The complete spatial and temporal discretization and further details are given in Ref. [28].

An essential prerequisite of the XDG method is a high-order accurate numerical integration of cut-cell integrals, such as integrals over cut-cell volumes and surfaces and integrals along the interface $\mathfrak{I}$. In this work we use the quadrature method proposed in Ref. [30].

The level-set field φ is represented by a standard DG approach, i.e., $\varphi(\boldsymbol{x}, t) = \sum_{j,n} \varphi_{j,n}(t)\Phi_{j,n}(\boldsymbol{x})$. In the context of the XDG method for transient two-phase flow problems, two level-set fields are introduced,

$$\varphi_{\text{evo}} \in \mathbb{P}_k(\mathfrak{K}_h) \quad \text{and} \quad \varphi \in \mathbb{P}_{k+1}(\mathfrak{K}_h) \cap C^0(\Omega), \tag{32}$$

where $\mathbb{P}_k(\mathfrak{K}_h)$ denotes the standard broken polynomial space of total degree k on the numerical mesh $\mathfrak{K}_h = \{K1, \dots, K_J\}$. The first one is used for handling the level-set evolution and the second one is used for the discretization, since the XDG method requires at least that $\varphi(\boldsymbol{x}, t) \in C^0(\Omega)$. Therefore,

it is given as the L^2 projection of φ_{evo} on the set of cut cells constrained by continuity conditions at the inner cell boundaries [28]. The polynomial degree is chosen to be $k + 1$.

For the level-set (interface) evolution given by

$$\frac{\partial \varphi_{\text{evo}}}{\partial t} + \boldsymbol{u}_{\text{ext}} \cdot \boldsymbol{\nabla} \varphi_{\text{evo}} = 0, \quad \text{on} \quad \Omega, \tag{33}$$

a suitable velocity field $\boldsymbol{u}_{\text{ext}}$ needs to be constructed from the bulk velocity $\boldsymbol{u}$ at the interface $\mathfrak{I}$. Different from the original work [28], the construction of the extension-velocity field $\boldsymbol{u}_{\text{ext}}$ is done via the solution of an auxiliary Stokes system of equations. Since $\boldsymbol{u}_{\text{ext}}$ is divergence-free, we can discretize scalar transport Eq. (33) in its conservative form and employ a standard upwind DG scheme. For further details we refer to Ref. [31].

In order to preserve the signed-distance property of the level-set field φ_{evo}, one may perform a reinitialization of φ_{evo} after a predefined number of time steps. In this case, the elliptic reinitialization problem in Ref. [32] is solved monolithically on the whole computational domain.

In this work, an explicit coupling between the interface evolution and the Navier-Stokes equations is employed. In this case, the interface is updated only once at the beginning. Note that, in this case, the surface tension force is also treated explicitly, and for the numerical computation of the surface tension force the Laplace-Beltrami formulation is used. The nonlinearity is solved via Picard iterations (convergence criterion set to 10^{-9}) and the preconditioned linear systems are solved using the direct solver MUMPS [33,34]. Further details on the solver structure and solution process are found in Ref. [25].

The presented method allows the use of local adaptive mesh refinement (AMR) during the simulation. At each so-called refinement level, a cell is divided into eight equal-sized subcells. The indication of the current refinement level of each cell is predefined; i.e., a fixed refinement level of either 1 or 2 is set for all cut cells and all cells in the narrow band (cells which share one face, edge, or vertex with cut cells). If the cut cells change due to interface motion, the refinement is adjusted accordingly.

V. RESULTS AND DISCUSSION

In this section we present results from our studies on nonlinear shape oscillations of viscous drops, using the WNLT and XDG methods. Results consist of the oscillation frequency as a function of the deformation parameter and the drop aspect ratio as well as energy-based parameters as functions of time.

The WNLT describes the flow field variables and the drop surface by series expansions truncated after the third order. The third approximation order is needed, since the nonlinear effects are not properly represented by the second order [3]. Due to the truncation, conservation of the drop volume during the oscillatory motion is not guaranteed [2,3,35]. The relative deviation of the deformed drop volume from the correct nondimensional value $V_s = 4\pi/3$ is calculated analytically. The nondimensional drop volume $V(t)$ is given as

$$V(t) = \frac{2\pi}{3} \int_{-1}^{1} r_s^3(\theta, t) d\cos\theta \approx \frac{2\pi}{3} \int_{-1}^{1} \left[1 + \eta_1(\theta, t)\eta_0 + \eta_2(\theta, t)\eta_0^2 + \eta_3(\theta, t)\eta_0^3 \right]^3 d\cos\theta. \tag{34}$$

The relative volume deviation from the correct value $R(\eta_0, t)$ is defined as follows:

$$R(\eta_0, t) =: \frac{V(t) - V_s}{V_s} = \frac{1}{2} \int_{-1}^{1} \left[r_s^3(\theta, t) - 1 \right] d\cos\theta. \tag{35}$$

Figure 2 presents $R(\eta_0, t)$ as a function of the deformation parameter for the modes of initial deformation $m = 2, 3,$ and 4 at the time instance $t = t_{\max}$ of the largest volume deviation. The drop Ohnesorge number is $Oh = 0.1$. The values of R are all positive and increase with the deformation
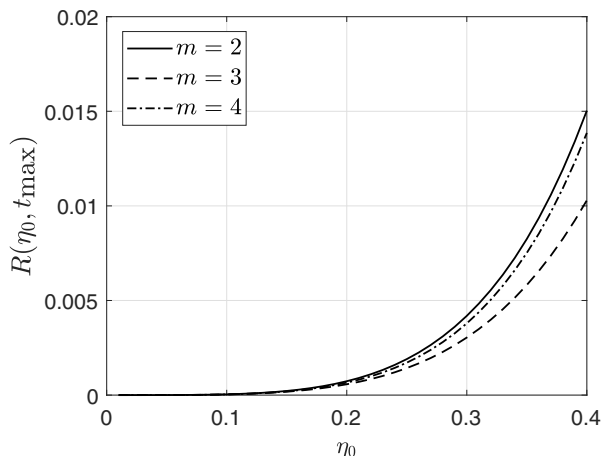
FIG. 2. Maximum relative drop volume deviation of the WNLT from the exact value for initial modes of deformation $m = 2$, 3, and 4 at $Oh = 0.1$ as a function of the deformation parameter η_0.

parameter η_0. For deformation parameters $\eta_0 \leqslant 0.4$, the maximum volume deviation for all the modes considered is 1.5%. For the comparison between the WNLT and XDG methods, we therefore consider initial deformations up to $\eta_0 = 0.4$ only, thus keeping the relative volume deviation low. The relative volume deviation of all the presented XDG simulations is below 0.11%, where the largest deviation is found for $m = 4$ and $\eta_0 = 0.7$.

The numerical setting for the XDG method is as follows: the computational domain is set to $\Omega = [0, 3R_0]^2 \times [-3R_0, 3R_0]$, which covers one-quarter of the simulated droplet, where the z axis is the symmetry axis. For all simulations, a base mesh of $7 \times 7 \times 14$ cells is taken, with additional adaptive mesh refinement of level 1 at the interface. The polynomial degrees for the velocity fields are set to $k = 3$ and $k - 1$ for the pressure field. In order to represent the dynamically inert ambient medium $\mathfrak{B}$ assumed for the WNLT, we set the inertia and viscous terms to a ratio of $1/1000$ compared to the droplet phase. This setting corresponds to an oscillating drop in a gaseous ambient medium with negligible momentum exchange, as seen with drops in streams produced by jet breakup or following gaseous flows with small relative velocity [36,37]. This approach was already taken in Ref. [38] for the direct numerical simulation of transient capillary rise, where the influence of the gaseous phase needs to be negligible. The time-step sizes δt are chosen such that the corresponding capillary time-step restriction is met given in dimensionless form by $\delta t < \delta t_\sigma = ((\frac{h_{\min}}{k+1})^3/(2\pi))^{1/2}$, where $h_{\min}$ denotes the smallest diameter of all cells.

In Fig. 3 the initial droplet shapes for all presented modes $m = \{2, 3, 4\}$ are depicted for their largest deformation parameter η_0, i.e., $\eta_0 = 0.7$ for $m = 2$, $\eta_0 = 0.5$ for $m = 3$, and $\eta_0 = 0.7$ for $m = 4$. The brighter colored sections correspond to the domain simulated by the XDG method. On the right-hand side the whole computational domain is shown. One can see the background mesh with $7 \times 7 \times 14$ cells and the adaptive refinement by one additional level around the droplet. Note that the droplet shapes correspond to the continuous level-set field φ [cf. Eq. (32)] and are approximated by a polynomial degree of 4.

For characterizing the deformation of the droplet, we choose the aspect ratio L/W, where $L = r_s(0, t) + r_s(\pi, t)$ denotes the centerline length of the droplet and $W = 2r_s(\frac{\pi}{2}, t)$ the width in the equatorial plane $\theta = \pi/2$. This aspect ratio is studied as a function of time for various modes and degrees of initial deformation of the drop surface. For the results of the XDG method, we evaluate the aspect ratio via the summation of the droplet surface modes in terms of the Legendre polynomials $P_l(\cos\theta)$ [cf. Eq. (10)], obtained by mode decomposition for each time step t_i. This is
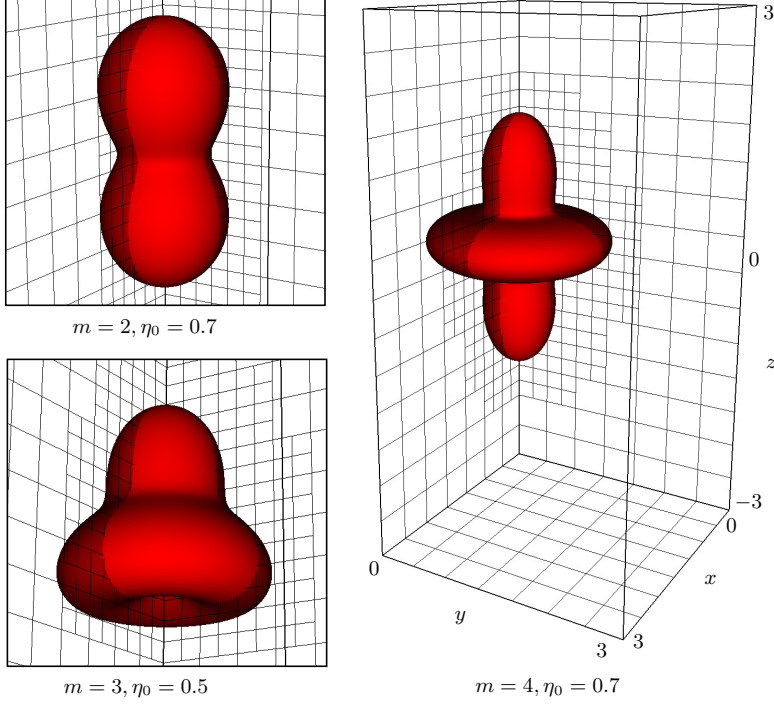
FIG. 3. Initial drop shapes and computational domain with adaptive mesh refinement for the XDG simulations. Left, top: $m = 2$ with $\eta_0 = 0.7$. Left, bottom: $m = 3$ with $\eta_0 = 0.5$. Right: whole computational domain for $m = 4$ with $\eta_0 = 0.7$.

done by minimizing

$$\oint_{\Im(t_i)} \left(\sum_l P_l(\cos\theta) a_l(t_i) - |\boldsymbol{x}| \right)^2 dS \to \min, \tag{36}$$

which is equivalent to requiring that

$$\oint_{\Im(t_i)} \left(\sum_l P_l(\cos\theta) a_l(t_i) - |\boldsymbol{x}| \right) P_n(\cos\theta) \, dS \stackrel{!}{=} 0 \quad \forall n, \tag{37}$$

where we assume that the droplet is axisymmetric. This leads to the following linear system of equations:

$$\sum_l \left(\oint_{\Im(t_i)} P_l(\cos\theta) P_n(\cos\theta) \, dS \right) a_l(t_i) = \oint_{\Im(t_i)} |\boldsymbol{x}| P_n(\cos\theta) \, dS \quad \forall n, \tag{38}$$

where a_l are the sought-after coefficients to the corresponding mode l. Thus, we evaluate $r_s(\theta, t_i) = \sum_l a_l(t_i) P_l(\cos\theta)$. Regarding the WNLT, the decomposition is based on the orthogonality of the Legendre polynomials with

$$a_l(t) = \left(l + \frac{1}{2} \right) \int_{-1}^1 \eta(x, t) P_l(x) \, dx, \quad \text{with} \quad x = \cos\theta. \tag{39}$$

In the following section, results from the two methods are compared for small to moderate deformation parameters $\eta_0 \leqslant 0.4$ (Sec. V A). Second, the drop shape oscillations are investigated

TABLE I. Simulation cases for the comparison between the XDG and the WNLT methods. For the initial velocity field, the term "stagnant" corresponds to zero velocity in both phases and "third order" corresponds to the internal droplet velocity field given by the WNLT. The values of $A(\theta)$ result from Eqs. (10) and (17).

Case	Oh	m	η_0	$A(\theta)$	δt	t_{end}	Initial velocity field
1.1	0.1	2	0.1	0.997981	5×10^{-3}	7	stagnant / third order
1.2	0.1	2	0.2	0.991848	5×10^{-3}	7	stagnant / third order
1.3	0.1	2	0.4	0.966781	5×10^{-3}	7	stagnant / third order
2.1	0.1	3	0.15	$0.996786 - 0.000315584 \cos\theta$	5×10^{-3}	7	stagnant / third order
2.2	0.1	3	0.4	$0.977143 - 0.00598442 \cos\theta$	5×10^{-3}	7	stagnant
3.1	0.1	4	0.1	0.998883	5×10^{-3}	7	stagnant / third order
3.2	0.1	4	0.4	0.981839	5×10^{-3}	7	stagnant
4	0.56	4	0.05	0.999721	5×10^{-3}	4	stagnant / third order

for larger deformation parameters up to 0.7, using the XDG method (Sec. V B). The presented results are available [39].

A. Comparison of the results from the XDG method and the WNLT

In Table I all simulation cases for the comparisons in this section are listed. Note that, for the comparison study, the two methods use the same parameter $A(\Theta)$ given in Eq. (10) for describing the initial drop shape. Another issue regards the initial velocity field. The WNLT predicts an internal velocity field when the drop is deformed to its initial shape. For the XDG method there are two options for the initial velocity field: set the velocity field up to the third-order contributions ("third order"), i.e., including first-, second-, and third-order solutions, given by the WNLT, or set a "stagnant" state with zero velocity throughout. The WNLT predicts the initial velocity field in the drop as a part of the solution, which is zero throughout in the inviscid case only. A discussion on the influence of the velocity field is given in Sec. V A 2.

1. Oscillation frequency and time spent in prolate shape (case 1)

One nonlinear effect known in oscillations is the dependency of the oscillation frequency on the oscillation amplitude. This effect occurs in drop shape oscillations also [2,3,8,40]. The frequency decreases with increasing oscillation amplitude. The results from the two simulation methods studied here, together with data from two pieces of literature, are shown in Fig. 4 (left) for a drop of $Oh = 0.1$ with mode of initial deformation $m = 2$. The resulting oscillation frequencies $\alpha_{\text{res,i}}$ are extracted from the traces of the drop north pole position $r_s(0, t)$ (see Appendix) and determined from the first oscillation period, between the first two maximum prolate shapes. The relative frequency change is calculated against the first-order oscillations frequency $\alpha_{2,\text{i}}$. The predictions from the present study are well in line with the data from the literature. The WNLT predicts a slightly stronger frequency decrease than all the other methods for initial aspect ratios L/W beyond 1.5, corresponding to $\eta_0 \geqslant 0.3$. The XDG results are in line with the numerical simulations of Ref. [9], while the finite-element-based simulations of Ref. [40] predict the weakest frequency decrease for a given initial deformation. Those authors used the commercial software package FIDAP, solving the Navier-Stokes equations with the Galerkin technique and advecting the free boundary with the spine method. The trend of the decrease of the oscillation frequency with increasing initial drop deformation, however, is predicted by all the methods.

The second well-known nonlinear effect describes the excess time of the drop spent in the prolate shape during one period. Again, the times are extracted from the drop north pole position during the first period. The results are compared to the same pieces of literature as before and depicted in Fig. 4 (right). The agreement between all the studies is very good throughout the whole range of initial aspect ratios. All methods show an increasing trend. The WNLT predicts slightly longer times,
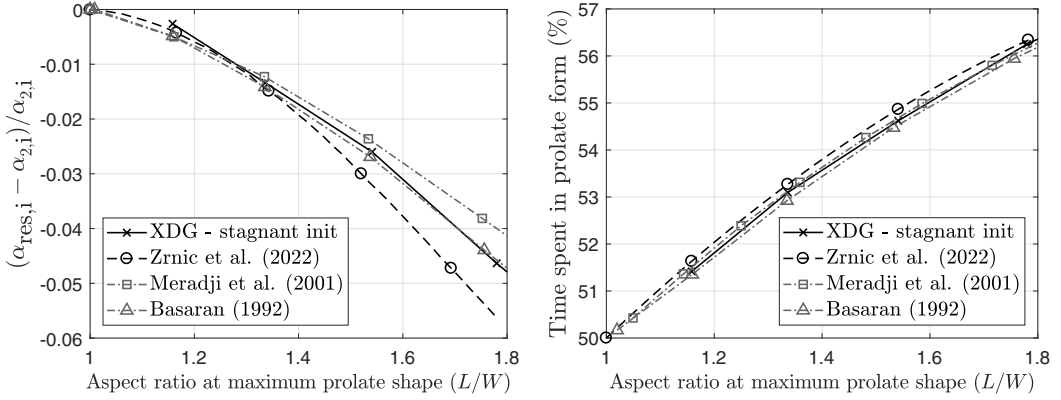
FIG. 4. Nonlinear effects for $Oh = 0.1$ and mode of initial deformation $m = 2$ for initial aspect ratios up to $L/W = 1.8$. Left: Frequency decrease as a function of the initial drop aspect ratio L/W. Right: Time percentage spent in prolate form as a function of the initial drop aspect ratio L/W.

whereas Ref. [9] predicts the shortest ones. The XDG results are well in line with the simulations of Ref. [41].

2. Drop aspect ratio over time (cases 1–3)

The XDG method offers the two above-mentioned options for the velocity field inside the droplet at the start of the oscillatory motion: the field inside the droplet may be initialized with zero velocity, i.e., in a stagnant state, or with the third-order velocity field given by the WNLT. The different resulting L/W as functions of time are shown, together with the results from the WNLT, in Fig. 5 for a drop with $Oh = 0.1$ at moderate deformations with $\eta_0 = 0.1$ and 0.2. The three different traces perfectly collapse, showing that the two methods of analysis agree very well for these moderate initial drop deformations. Zrnić *et al.* have shown that, in these oscillations, which are damped due to the drop viscosity, the oscillation frequency and the damping factor vary in time by no more than 0.7% and 3.7%, respectively [3].

Raising the initial deformation amplitude by setting $\eta_0 = 0.4$ yields the shape oscillations in Fig. 6. The results show that, with the increased initial deformation of the drop, the initial velocity field in the drop starts to make a significant difference. For a viscous drop liquid, the WNLT predicts
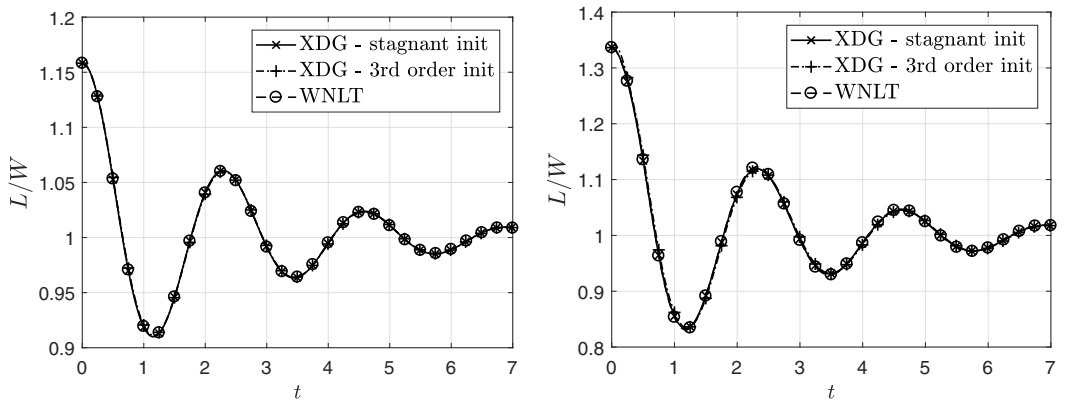

FIG. 5. Aspect ratio L/W over time for $Oh = 0.1$ and $m = 2$. Left: $\eta_0 = 0.1$ (case 1.1). Right: $\eta_0 = 0.2$ (case 1.2).
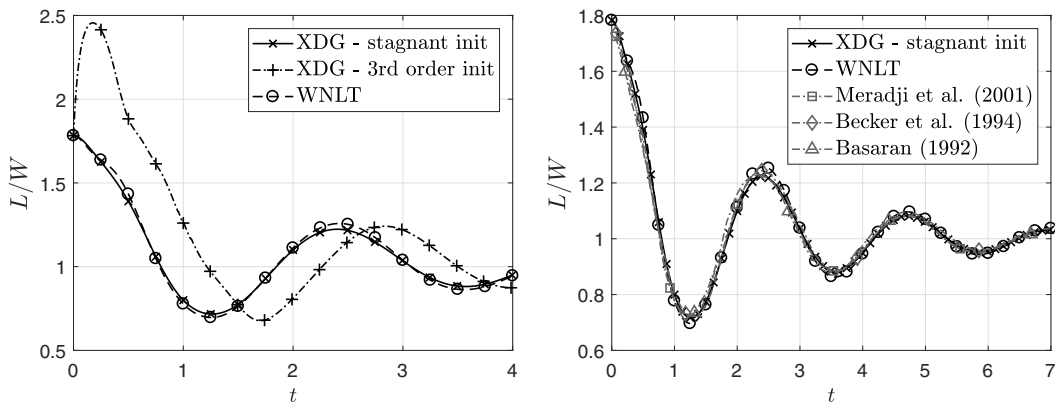
FIG. 6. Aspect ratio L/W over time for $Oh = 0.1$, $m = 2$, and $\eta_0 = 0.4$ (case 1.3).

an initial motion in the drop, since the initial conditions ensure a stagnant drop surface only in terms of its radial rate of displacement. However, the third-order initial velocity field leads to an overshoot at the beginning of the XDG simulation (see Fig. 6, left). A very small overshoot is also visible for $\eta_0 = 0.2$ (cf. Fig. 5, right). The reason for that might be the truncated power-series expansion of the velocity field up to third order [cf. Eq. (12)], which is sufficient to describe the motion of the droplet shape also described up to third order. Considering it as the initial velocity field for the three-dimensional XDG simulations, though, the third-order velocity field seems underresolved. This effect is confirmed by the data in Fig. 7, displaying for $Oh = 0.1$ and $m = 2$ the velocity magnitudes in the drops from the WNLT in the initial state, and the deviations of the XDG velocities therefrom, for the deformation parameters $\eta_0 = 0.2$ and 0.4. The deviations are seen to be one order of magnitude larger for the larger deformation parameter, with the large values in the polar regions of the drop. This effect indicates a limitation in the use of the WNLT velocity data at deformation parameters as large as 0.4. The larger the deformation parameter η_0, the larger the radial velocity components at the north and south poles of the droplet, driving the strong deformation at the start of the oscillation. Thus, in the remainder of this section, we restrict the comparison for the third-order initial velocity field to the cases with the smallest η_0. Figure 7 also shows two initial velocity fields in drops deformed according to $m = 2$ by magnitude and as vector fields. The fields exhibit two toroidal structures with zones around the drop poles separated from them. These zones are more pronounced at stronger initial deformation. Considering the stagnant initial velocity field, the XDG simulation is in very good agreement with the WNLT. The largest deviations occur shortly after the start of the motion (around $t = 0.4$) and the local extrema of the trace. This may be explained by the differences between the initial states of the drop bulk. Again, we compare to Refs. [9,41], and further to Ref. [37], which used experimental data and numerical calculations for the investigations. The results are shown on the right of Fig. 6. All results agree very well throughout the time range, where the WNLT predicts on all extrema slightly higher (respectively lower) values than the others.

In addition to the evolution of the aspect ratio over time, we present a shape comparison between XDG (stagnant initial velocity field) and WNLT in Fig. 8. Just as for the aspect ratio, the depicted drop shapes for the XDG approach are evaluated via the summation of the droplet surface modes [cf. Eq. (38)]. In Fig. 8 (left), an excellent agreement for the initial maximum deformation is shown. In Fig. 8 the first minimum and maximum after the initial maximum are depicted. Note that for each method the corresponding instance in time is presented, i.e., $t = 1.26$ (XDG) and $t = 1.25476$ (WNLT) for the minimum and $t = 2.405$ (XDG) and $t = 2.42237$ (WNLT) for the second maximum. As described for the aspect ratio evolution above, the XDG method predicts slightly higher (lower) values for the minima (maxima) compared to the WNLT. Considering the
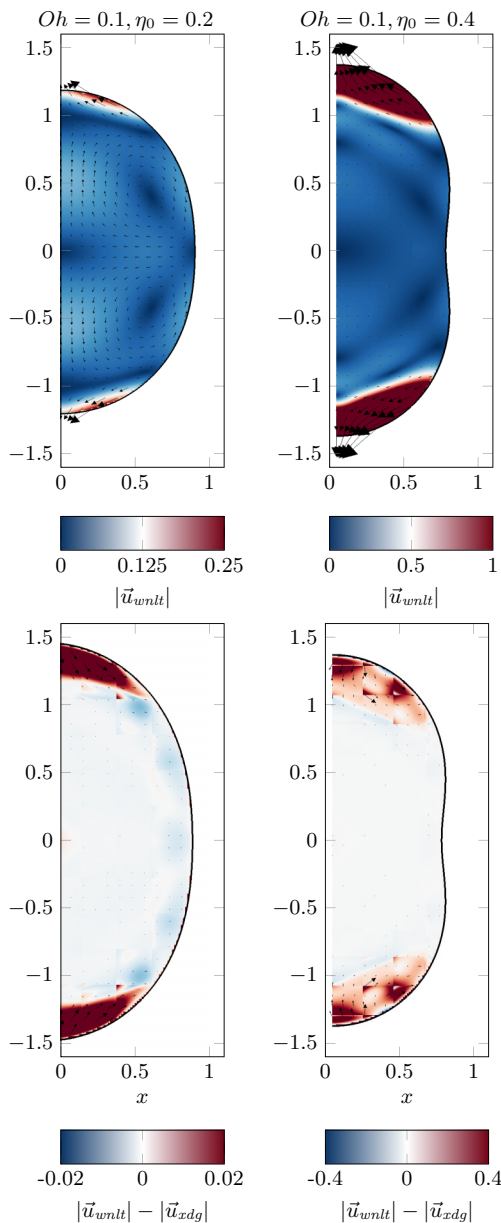
FIG. 7. Initial velocity magnitude from the WNLT (top) and deviation of the initial XDG velocities therefrom (bottom), for $\eta_0 = 0.2$ (left) and $\eta_0 = 0.4$ (right). Mode of initial deformation $m = 2$, $Oh = 0.1$.

instances of time, the minima for the XDG method occur shortly after the WNLT and vice versa for the maxima. Overall, the agreement for the droplet shapes between both methods is very good.

Next we study the evolution of the drop aspect ratio for the mode of initial deformation $m = 3$. The data are shown in Fig. 9 for a drop with $Oh = 0.1$ with the two values of the deformation parameter $\eta_0 = 0.15$ and 0.4. The results from the three analyses agree very well, showing the influence from a higher-order mode, to which $m = 3$ couples in the motion briefly after start. The result is a quasiperiodicity of the motion. This mode is strongly damped, leaving a periodic motion,
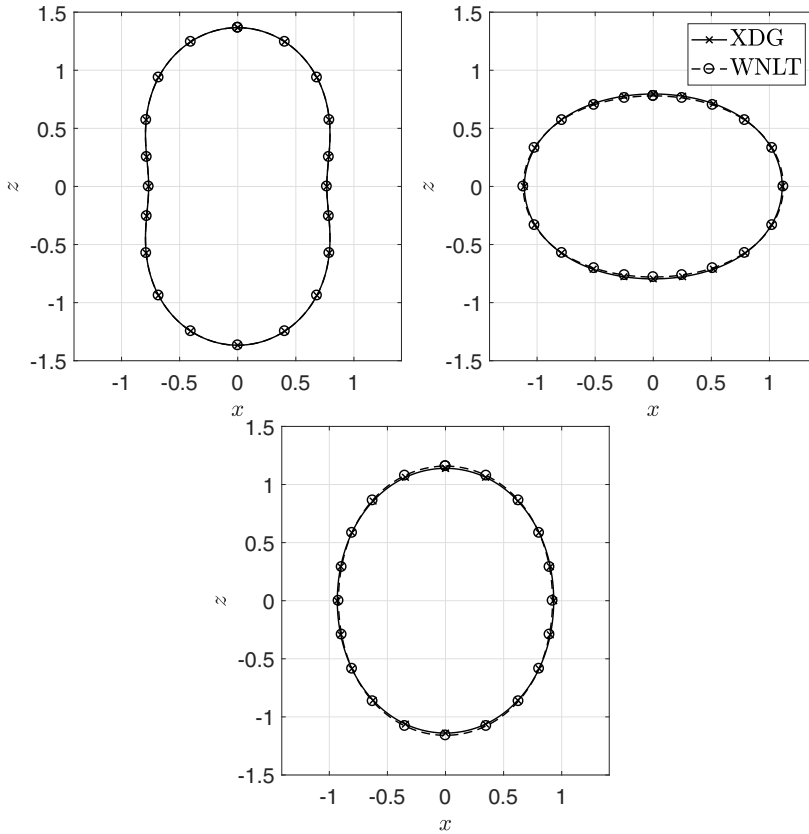
FIG. 8. Droplet shape comparison for $Oh = 0.1$, $m = 2$, and $\eta_0 = 0.4$ (case 1.3) at time instances corresponding to the first three extreme values of the aspect ratio evolution (cf. Fig. 6, left). Left: Initial maximum deformation at $t = 0$. Right: Minimum deformation at $t = 1.26$ for the XDG approach and at $t = 1.25476$ for WNLT. Bottom: Maximum deformation at $t = 2.405$ for the XDG approach and at $t = 2.42237$ for WNLT. XDG computations have initially stagnant drop.
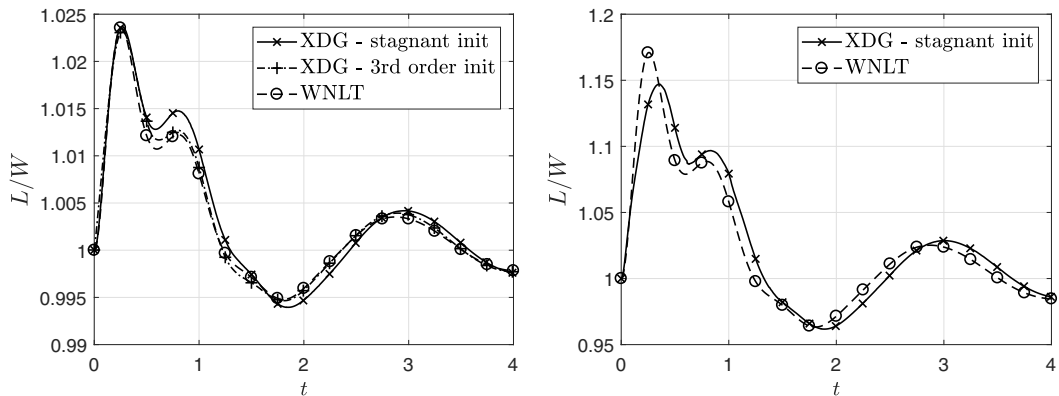

FIG. 9. Aspect ratio L/W over time for $Oh = 0.1$ and $m = 3$. Left: $\eta_0 = 0.15$ (case 2.1). Right: $\eta_0 = 0.4$ (case 2.2).
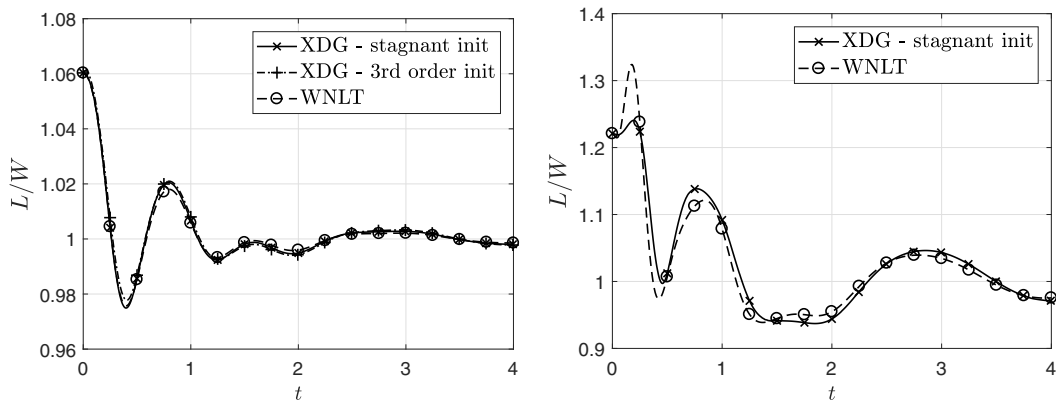
FIG. 10. Aspect ratio L/W over time for $Oh = 0.1$ and $m = 4$. Left: $\eta_0 = 0.1$ (case 3.1). Right: $\eta_0 = 0.4$ (case 3.2).

approximately from around $t = 2$ on. The details of the quasiperiodic motion of the drop surface agree very well between the different methods of analysis, even for the stronger deformation at $\eta_0 = 0.4$. Note that for the XDG simulation with the third-order initial velocity field in Fig. 9 (left), the agreement with the WNLT is much better than with the stagnant velocity field.

Studying a drop with the initial mode of deformation $m = 4$ for two different values of the deformation parameter yields the results in Fig. 10. The findings are similar to those at mode $m = 3$, in that the data from the different methods of analysis agree very well. At the higher value $\eta_0 = 0.4$, however, the initial velocity field in the drop predicted by the WNLT in the early periods of the motion makes a stronger difference against the XDG results than with $m = 3$. The quasiperiodicity of the motion remains present for a longer period of time than with mode $m = 3$, indicating the coupling to less strongly damped (lower-order) modes for $m = 4$. The agreement between the WNLT and the XDG results in terms of the traces in time is remarkably good.

For the drop shape oscillations studied, we are interested in the oscillation frequencies involved in the motions. For quantifying this, we compute the Fourier power spectra of the frequency involved in the data traces in time. The finite time spectra of a function of time $g(t)$ are given as

$$\hat{g}(\alpha) = \int_{t_1}^{t_2} g(t)e^{-i\alpha t}dt \quad \text{and} \quad \hat{g}_d(\alpha) = \frac{1}{N}\sum_{n=1}^{N} g(t_n)e^{-i\alpha t_n} \tag{40}$$

in an analytical form, for use with the analytical solutions from the WNLT, and in a discrete form, using the numerical data from the XDG method, respectively. In the discrete form, N is the number of time instants between the times t_1 and t_2. The Fourier transform becomes more important for finding the frequencies, the more the quasiperiodicity influences the time series in motions with large deformations. The frequencies are then not easily found from a "manual" inspection of the traces. Figures 11–13 show the normalized Fourier power spectra of the frequency for the motions of the drop north pole corresponding to the data on the left in Figs. 6, 9, and 10, respectively. The corresponding plots for the drop north pole position as a function of time are found in the Appendix A 1. The spectra exhibit zero values at zero frequency, because the underlying data represent the deviations of the north-pole position from its time average. The spectra are shown as obtained from an analysis of the first oscillation period only, and from analyzing the period of time $0 \leqslant t \leqslant 7$ in order to see the evolution of the frequency spectra with ongoing time during the oscillations.

For all the oscillating drops studied, the analytical and computational methods yield nearly identical power spectra of the oscillation frequency, as represented in the diagrams by the dashed and solid lines, respectively. The spectra of the first oscillations exhibit peaks at frequencies deviating
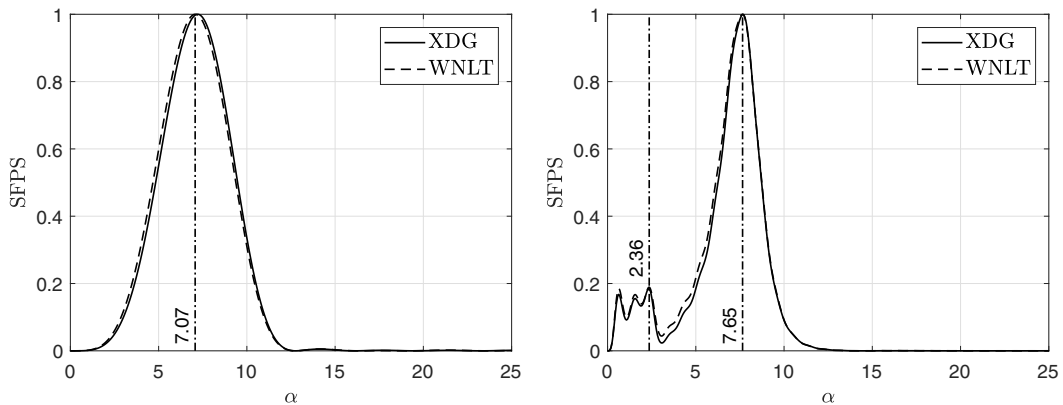
FIG. 11. Squared real parts of the Fourier power spectra of the oscillation frequency for the drop north pole motion corresponding to the left-hand side of Fig. 6 from XDG and WNLT, normalized with the respective maximum values (SFPS), for $Oh = 0.1$, $m = 2$, and $\eta_0 = 0.4$: left, results for the first oscillation; right, results for the interval $0 \leqslant t \leqslant 7$.

from the solutions of the characteristic equation of the drop, i.e., from the linear oscillation frequency. The deviations of the peak frequencies for the first oscillation period from the corresponding solution of the characteristic equation of the drop are -13%, -8.6%, and -10% for $m = 2$ at $\eta_0 = 0.4$, for $m = 3$ at $\eta_0 = 0.15$, and for $m = 4$ at $\eta_0 = 0.1$, respectively. For a given initial degree of deformation, the frequency deviation, indicating nonlinear oscillatory behavior, increases with the mode of initial deformation. It is particularly large for the present case in the fundamental mode, since the initial deformation with $\eta_0 = 0.4$ is large enough to cause this. For the longer time intervals covered by the Fourier transform, the differences are smaller in absolute value throughout (-5.8%, -2.3%, and -2.6%, respectively), since the damping of the oscillation, which reduces the deformation amplitudes in time, brings the drops closer to the linear behavior. The spectra are narrower around the dominant frequency for the longer integration time than for the first oscillation alone. The spectra furthermore exhibit secondary peaks at frequencies higher or lower than the dominant one. For the data from the first oscillation period at $m = 2$, secondary peaks at higher

FIG. 12. Squared real parts of the Fourier power spectra of the oscillation frequency for the drop north pole motion corresponding to the left-hand side of Fig. 9 from XDG and WNLT, normalized with the respective maximum values (SFPS), for $Oh = 0.1$, $m = 3$, and $\eta_0 = 0.15$: left, results for the first oscillation; right, results for the interval $0 \leqslant t \leqslant 7$.

FIG. 13. Squared real parts of the Fourier power spectra of the oscillation frequency for the drop north pole motion corresponding to the left-hand side of Fig. 10 from XDG and WNLT, normalized with the respective maximum values (SFPS), for $Oh = 0.1$, $m = 4$, and $\eta_0 = 0.1$: left, results for the first oscillation; right, for the interval $0 \leqslant t \leqslant 7$.

frequency appear at $\alpha = 4.58$ and at $\alpha = 7.05$. The latter deviates from the frequency for $m = 4$, with which $m = 2$ couples, by no more than -0.3%. In contrast, the former is close to the difference between the peak frequency and the secondary peak at $\alpha = 7.05$, which characterizes this as a beat frequency. For $m = 3$, secondary peaks with very low power densities appear at $\alpha = 9.34$ and at $\alpha = 11.8$. The latter deviates from the frequency for $m = 5$ by no more than 10%, while the former is close to the difference between the peak frequency and the frequency for $m = 2$, with which $m = 3$ couples at third order. For $m = 4$, there exists one secondary peak with very low power density at $\alpha = 14.2$, which deviates from the corresponding solution of the characteristic equation of the drop by no more than 2.8%. Even higher frequencies are even less represented in the power spectrum.

The spectra evaluated for the time interval $0 \leqslant t \leqslant 7$ exhibit secondary peaks below the dominant peak frequency. These frequencies may be interpreted as beat frequencies throughout, which develop with ongoing time and are therefore not visible in the first oscillation period. The frequency of 0.6 appears in all the three spectra, and values around 1.56 and 2.4 are found in the spectra for $m = 3$ and $m = 4$. The oscillations from the first period interact with those developing later in time.

3. Oscillatory motion starting from a supercritical state (case 4)

As a final item, we study the motion of a drop with the relatively large Ohnesorge number $Oh = 0.56$, which is initially deformed at mode $m = 4$. For this drop, the characteristic equation predicts a zero oscillation frequency; i.e., the drop is in this sense supercritical. The linear theory therefore predicts aperiodic behavior, i.e., that the drop returns from its deformed initial state to the spherical state without oscillating. The WNLT, however, predicts the damped periodic oscillations of this drop, in agreement with the XDG analysis accounting for the initial velocity field from the WNLT. The data are shown in Fig. 14. In contrast to this, the XDG approach starting from a stagnant drop predicts aperiodic behavior.

The reasons for this behavior are found by decomposing the drop shape into the contributing modes as functions of time, as shown in Fig. 15. The diagrams show the coefficients a_l in the modal expansion of the drop shape as functions of time, exhibiting significant contributions from modes $l = 2$ and $l = 4$. This shows that the WNLT analysis starts from a state of motion inside the drop where mode coupling has excited mode $l = 2$. For this mode, the drop at this Ohnesorge number exhibits damped periodic oscillations. The high Ohnesorge number leads to strong dampening of the oscillation. The oscillation therefore dies out rapidly, as seen in Fig. 14. The modes $l = 0$ and $l = 6$
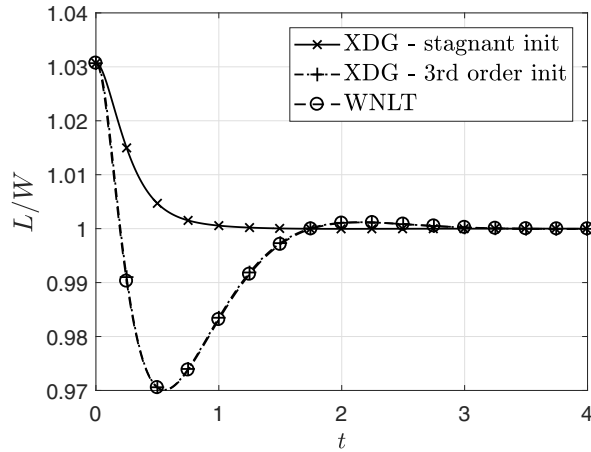
FIG. 14. Aspect ratio L/W over time for $Oh = 0.56$, $m = 4$, and $\eta_0 = 0.05$. The linear theory predicts an aperiodic motion.

contribute by coefficients with values one to two orders of magnitude smaller than a_2 and a_4. The initially stagnant drop, in contrast, exhibits very small values of a_2 at all times, since, when starting from rest, mode coupling does not have the time to produce strong shape deformations against the effect of dampening. This is the reason for the seemingly aperiodic drop behavior predicted by the XDG method when starting from the drop at rest.
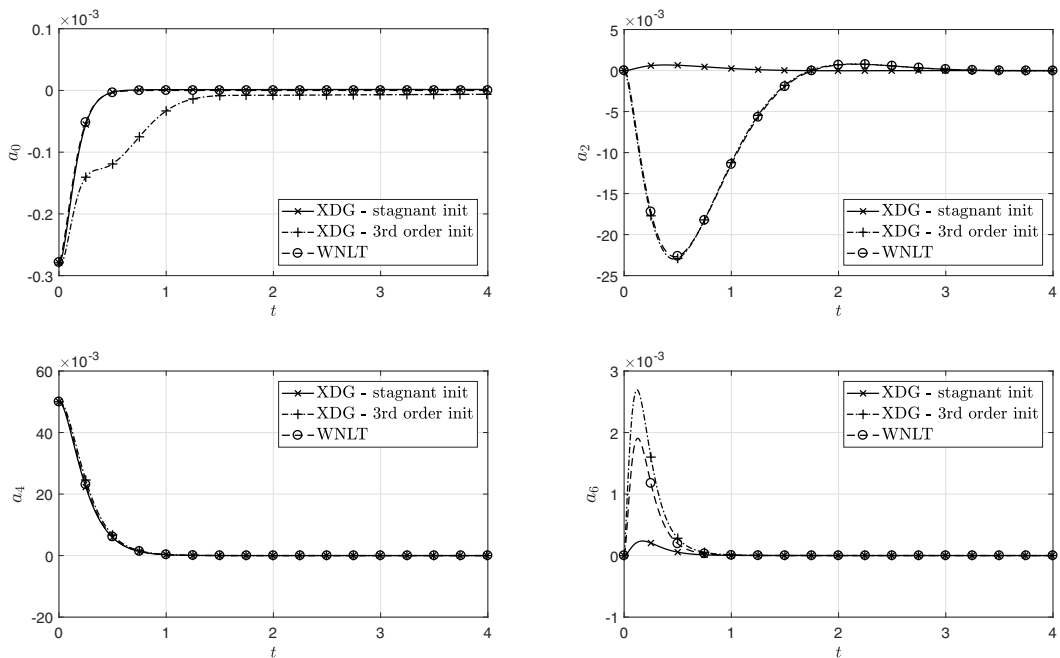
FIG. 15. Mode decomposition of the drop surface as a function of time for $Oh = 0.56$, $m = 4$, and $\eta_0 = 0.05$, represented by the coefficients of the series expansion of the drop surface shape.

TABLE II. Additional simulation cases of large-amplitude oscillations up to $\eta_0 = 0.7$ using the XDG method. The Ohnesorge number $Oh = 0.1$, and the initial velocity field is stagnant. Time step $\delta t = 5 \times 10^{-3}$; simulations to time $t_{\text{end}} = 4$.

Case	m	η_0	$A(\Theta)$
1.4	2	0.3	0.981486
1.5	2	0.5	0.947538
1.6	2	0.6	0.923706
1.7	2	0.7	0.895131
2.3	3	0.3	$0.987143 - 0.00252468 \cos\theta$
2.4	3	0.5	0.964301
3.3	4	0.2	0.995508
3.4	4	0.3	0.989838
3.5	4	0.5	0.971459
3.6	4	0.6	0.958674
3.7	4	0.7	0.943440

B. Large-amplitude study by the XDG method

The XDG method allows drop shape oscillations to be studied up to large amplitudes of deformation. This method is therefore used to investigate strongly nonlinear axisymmetric drop shape oscillations at large deformation, corresponding to values of the deformation parameter η_0 up to 0.7. Table II lists the additional simulation cases for the large-amplitude study in this section. All simulations are initialized with a stagnant velocity field.

1. Oscillation frequency and time spent in prolate shape (case 1)

In Sec. V A 1 we compared the two presented methods, WNLT and XDG, up to a deformation parameter of $\eta_0 = 0.4$, i.e., an initial aspect ratio of $L/W < 1.8$ (cf. Fig. 4). In this section we extend this figure, showing the nonlinear effects up to $L/W < 3$ and comparing against Refs. [9,41]. Looking at the frequency change [Fig. 16(a)], we observe an excellent agreement with the results of Ref. [9], where both describe a slightly curved trace starting from $L/W = 1.5$. Reference [41] predicts a more linear and weaker frequency decrease for larger initial deformations. In Fig. 16(b)
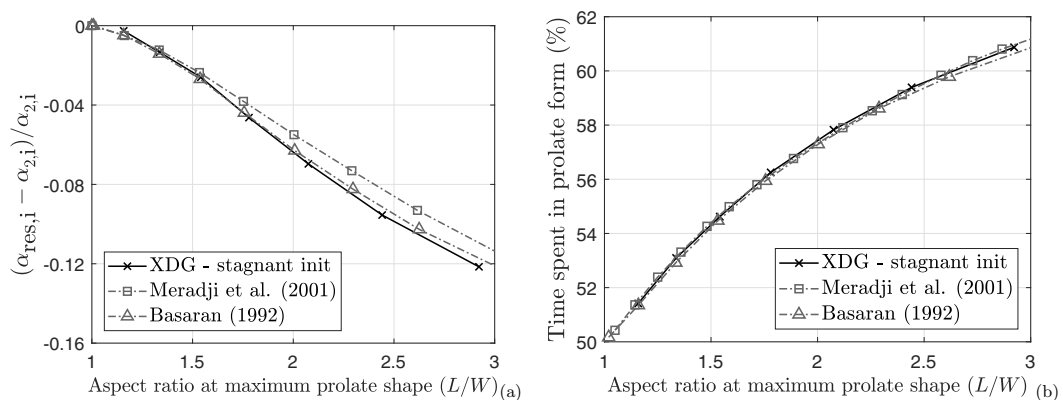
FIG. 16. Nonlinear effects for $Oh = 0.1$ and mode of initial deformation $m = 2$ for initial aspect ratios up to $L/W = 3$. (a) Frequency decrease as a function of the initial drop aspect ratio L/W. (b) Time percentage spent in prolate form as a function of the initial drop aspect ratio L/W.
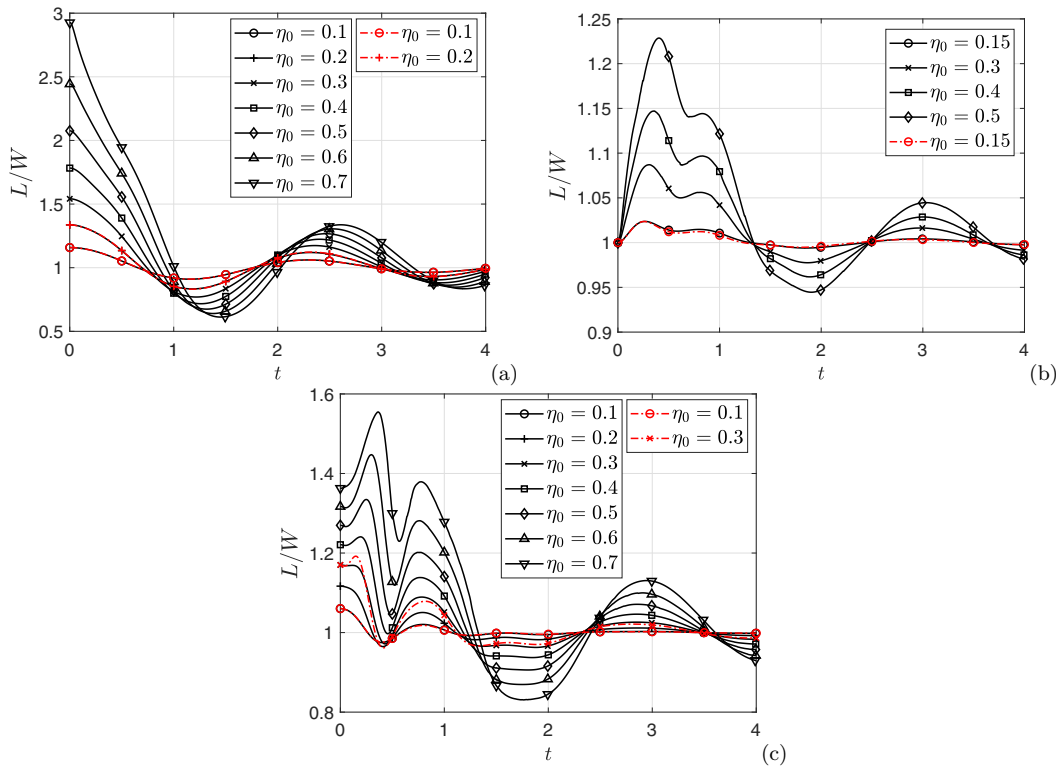
FIG. 17. Aspect ratio L/W over time t for drops with $Oh = 0.1$ in the different modes of initial deformation (a) $m = 2$, (b) $m = 3$, and (c) $m = 4$, with deformation parameters up to $\eta_0 = 0.7$. The red dash-dotted lines indicate WNLT results.

we present the extended plot for the time percentage spent in prolate form. Here, all the results coincide very well throughout the whole range of aspect ratios L/W.

2. Aspect ratio over time (cases 1–3)

In Fig. 17 we present the drop aspect ratio as a function of time for the three modes $m = \{2, 3, 4\}$ of initial deformation studied in this paper. The traces for $m = 2$ and $\eta_0 = \{0.1, 0.2, 0.4\}$ were shown in Figs. 5 and 6 already, for $m = 3$ and $\eta_0 = \{0.15, 0.4\}$ in Fig. 9, and for $m = 4$ and $\eta_0 = \{0.1, 0.4\}$ in Fig. 10. The red dash-dotted lines indicate WNLT results for the deformation parameters given in the legends. Note that, for $m = 3$ and $\eta_0 = 0.5$, a level-set reinitialization is performed every 50th time step (cf. Sec. IV).

The traces of the drop aspect ratio in time show that the quasiperiodicity of the oscillations arising with increasing deformation is more pronounced for the higher modes of initial deformation. This result is confirmed by the WNLT data. The reason is that higher modes couple to lower modes with smaller oscillation frequency, which influence the traces in time more visibly and survive longer in time due to the smaller damping factor. This is clearly seen in Fig. 17(c) for $m = 4$. From $\eta_0 = 0.4$ on, the trend of deformation of the drop after the start of the motion even changes its sign, leading to a further elongation of the drop rather than a contraction. The long living mode $m = 2$ then leads to a trace of the aspect ratio in time, which is markedly different from the ones for $\eta_0 \leqslant 0.3$, taking to times beyond $t = 1.5$ to return to a harmonic oscillation.

The Fourier transforms of the motions of the drop north pole, corresponding to the evolutions of the aspect ratio in time and found in Appendix A 2, again reveal the frequency power density
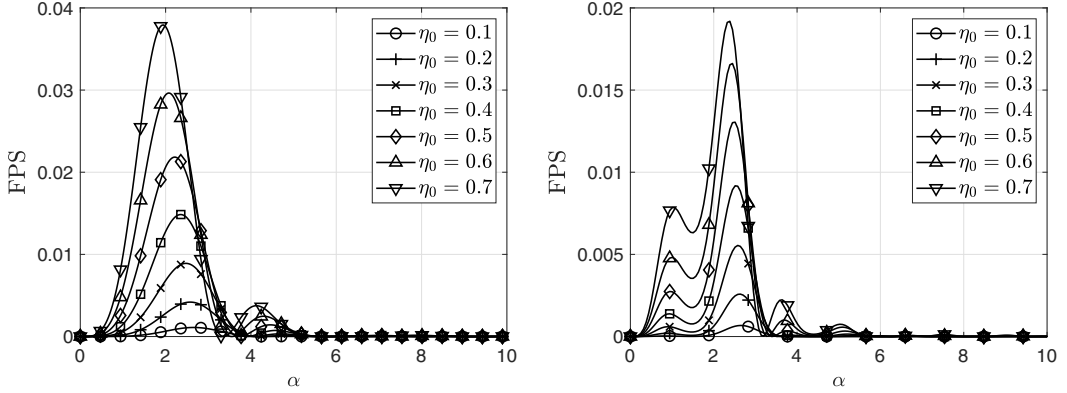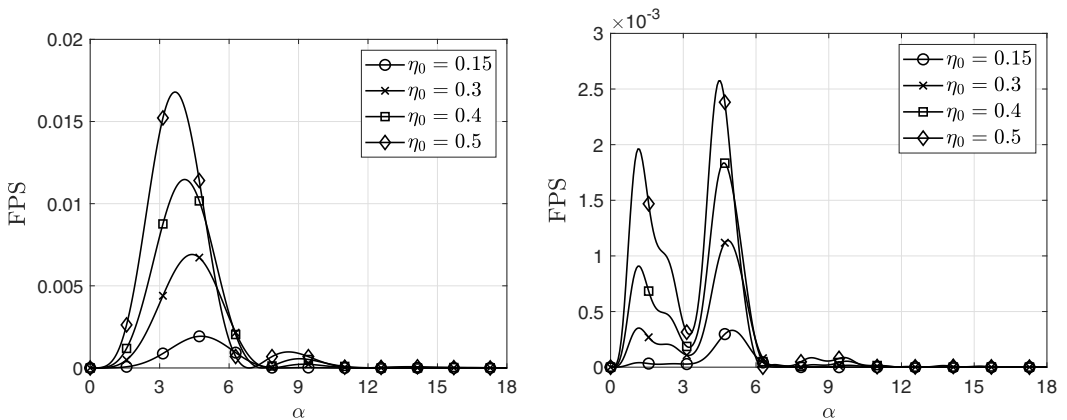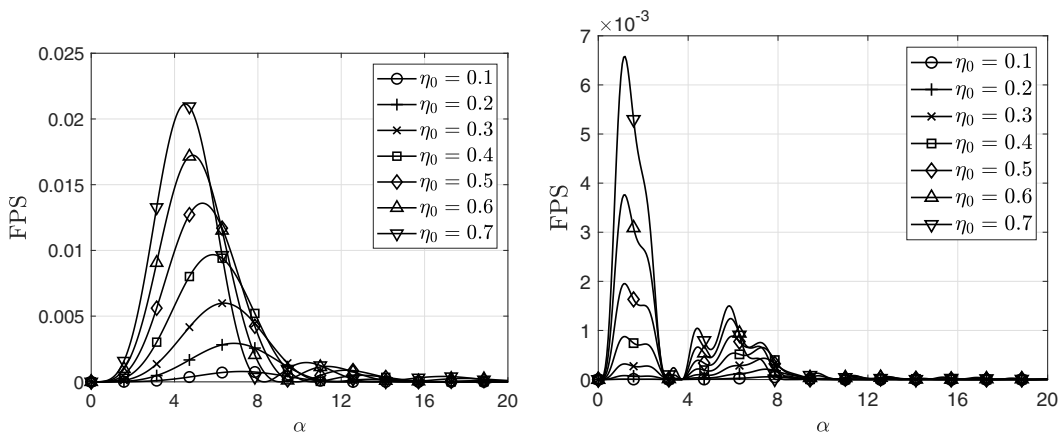
FIG. 18. Squared real parts of the Fourier power spectra (FPS) of the oscillation frequency for the drop north pole motion corresponding to Fig. 17(a) for $Oh = 0.1$, $m = 2$, and varying η_0: results on the left for the first oscillation and on the right for the interval $0 \leqslant t \leqslant 4$.

in the data. The spectra shown in Figs. 18–20 for the modes of initial drop deformation $m = 2$ through $m = 4$ were again obtained for the first oscillation (left-hand diagrams) and for a longer time interval (right-hand diagrams), which is $0 \leqslant t \leqslant 4$ in the present figures. The spectra are not normalized, in order to show the higher power densities for the stronger deformations. The peak frequencies decrease with increasing initial deformation, as expected from the known nonlinear behavior of the drops at lower deformation. The data from the first oscillation period show that, for $m = 2$, the peak frequency decreases from $\alpha = 2.67$ to $\alpha = 1.95$, i.e., by -27%, as η_0 increases from 0.1 to 0.7. For $m = 3$, the corresponding frequency decrease is -23% between $\eta_0 = 0.15$ and 0.5, and for $m = 4$ it is -37% between $\eta_0 = 0.1$ and 0.7. This strong influence of the large deformations on the oscillation frequency was expected. Secondary peaks appear for mode coupling and as beats between the different oscillation mode frequencies, as with the smaller deformations discussed above.

FIG. 19. Squared real parts of the Fourier power spectra (FPS) of the oscillation frequency for the drop north pole motion corresponding to Fig. 17(b) for $Oh = 0.1$, $m = 3$, and varying η_0: results on the left for the first oscillation and on the right for the interval $0 \leqslant t \leqslant 4$.

FIG. 20. Squared real parts of the Fourier power spectra (FPS) of the oscillation frequency for the drop north pole motion corresponding to Fig. 17(c) for $Oh = 0.1$, $m = 4$, and varying η_0: results on the left for the first oscillation and on the right for the interval $0 \leqslant t \leqslant 4$.

3. Energies over time (cases 1–3)

In this section, the resulting velocity fields and the position of the interface obtained by the XDG simulations are used to quantify the kinetic energy,

$$E_{\text{kin}} = \frac{1}{2} \int_{\mathfrak{A}} \boldsymbol{u} \cdot \boldsymbol{u} \, dV, \tag{41}$$

the deviation of the surface energy from the spherical state,

$$\Delta E_{\text{surf}} = \int_{\mathfrak{I}} 1 dA - 4\pi, \tag{42}$$

and the corresponding deviation of the total energy,

$$\Delta E_{\text{tot}} = E_{\text{kin}} + \Delta E_{\text{surf}}, \tag{43}$$

of the drop. Note that the presented quantities above are calculated for the whole drop from the XDG simulations, which are performed on the quarter domain. The kinetic energy was derived from the WNLT results as

$$E_{\text{kin,WNLT}} = \frac{1}{2} \int_{\mathfrak{A}} \left[(\boldsymbol{u}_1 \cdot \boldsymbol{u}_1) \eta_0^2 + 2(\boldsymbol{u}_1 \cdot \boldsymbol{u}_2) \eta_0^3 \right] dV. \tag{44}$$

In Fig. 21, the bulk kinetic energy of the oscillating drop with $Oh = 0.1$ is depicted as a function of time for the three different modes of initial deformation studied. The red dash-dotted curve in Fig. 21(a) shows the results from the WNLT at $\eta_0 = 0.1$, which collapse on the related XDG data. The energy evolution starts from zero, since the drop is initiated in a stagnant, deformed state. The kinetic energy exhibits the expected behavior, but with a less visible quasiperiodicity at the higher deformation amplitudes than seen in the drop aspect ratio traces. This holds particularly for $m = 4$. The reason is the influence from the squared velocity, which affects the time behavior, showing a doubling of the frequency against the traces for the aspect ratio.

Figure 22 depicts the surface energy traces for the four different modes of initial deformation corresponding to the deformation of the drop against the spherical state. The evolutions start from the initial surface energy, corresponding to the state of deformation and the deformation mode. The red dash-dotted curve in Fig. 22(a) shows the results from the WNLT at $\eta_0 = 0.1$, which collapse on the related XDG data. At a given value of the deformation parameter η_0, the higher modes
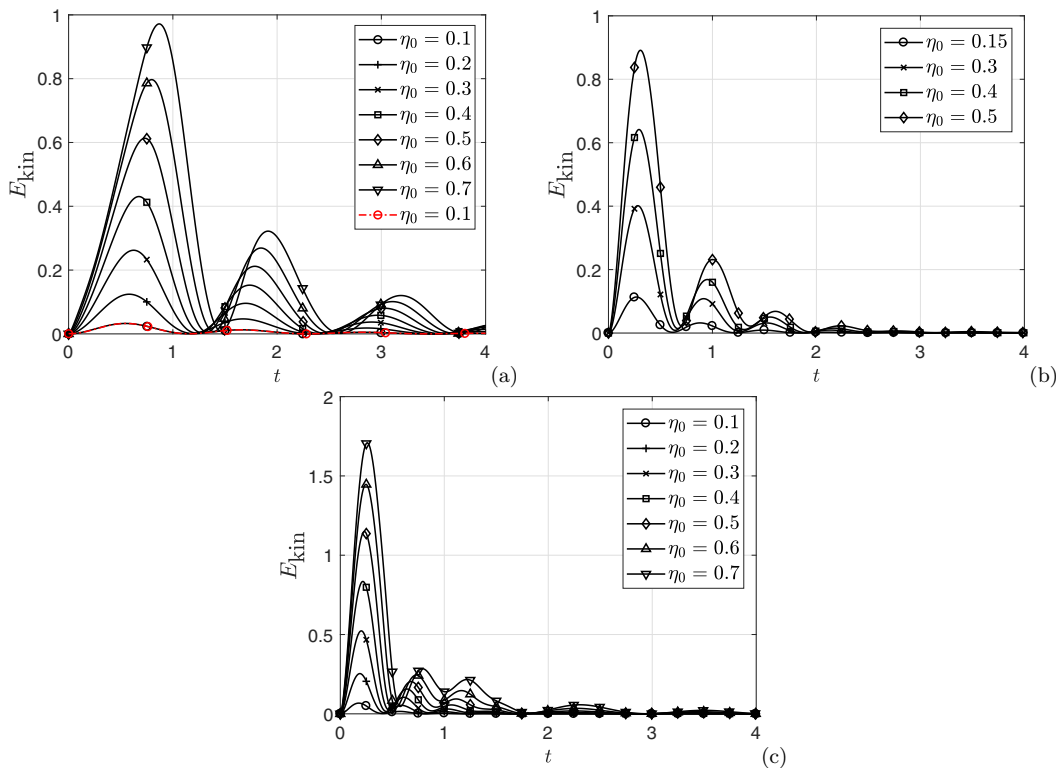
FIG. 21. Kinetic bulk energy $E_{\text{kin}} = \frac{1}{2} \int_{\mathfrak{A}} \boldsymbol{u} \cdot \boldsymbol{u} \, dV$ over time t for the different modes of initial deformation (a) $m = 2$, (b) $m = 3$, and (c) $m = 4$, with deformation parameters up to $\eta_0 = 0.7$ and Ohnesorge number $Oh = 0.1$. The red dash-dotted line indicates WNLT results.

of deformation involve higher surface energies. The corresponding damping factor also increases with the mode of deformation, leading to a steeper decay of the energy in time for the higher than for the lower modes. At the stronger deformations for the modes $m \geqslant 3$, furthermore, the kinetic and surface energies do not reach the values of zero at the first minima. For $m = 3$ this is visible from $\eta_0 = 0.3$ on, and for $m = 4$ from $\eta_0 = 0.4$. This means that the drop surface energy is not totally converted into kinetic energy when the latter reaches its first maximum, and vice versa at the first minimum of the surface energy. This finding was reported in Ref. [2] for inviscid drops at higher-order deformation modes and strong deformations also.

In the present context, the sum of the two above-discussed forms of mechanical energy of the drop is denoted as the total energy. The total energy has the tendency to decrease in time, which is due to dissipation of the mechanical energy into heat. The effect on the drop liquid from the dissipation is not accounted for in the present study. The decay of the total energy is, therefore, not to be seen as a conflict with energy conservation. The data from the XDG simulations in Fig. 23 show that the rate of total energy decay is highest at times of largest velocities. The strong motion inside the drop goes along with high shear rates in the drop, which govern the rate of dissipation. Consequently, the high kinetic energies at mode $m = 4$ lead to a rapid decay of the total energy, as seen in Fig. 23(c). The red dash-dotted curve in Fig. 23(a) shows the results from the WNLT at $\eta_0 = 0.1$, which collapse on the related XDG data. For a given deformation parameter, the large damping factors at the higher-order modes of deformation can, therefore, be attributed to the higher energies associated to the initial state of deformation of the drop. The increase of damping factor with the mode number is seen in the linear theory also.
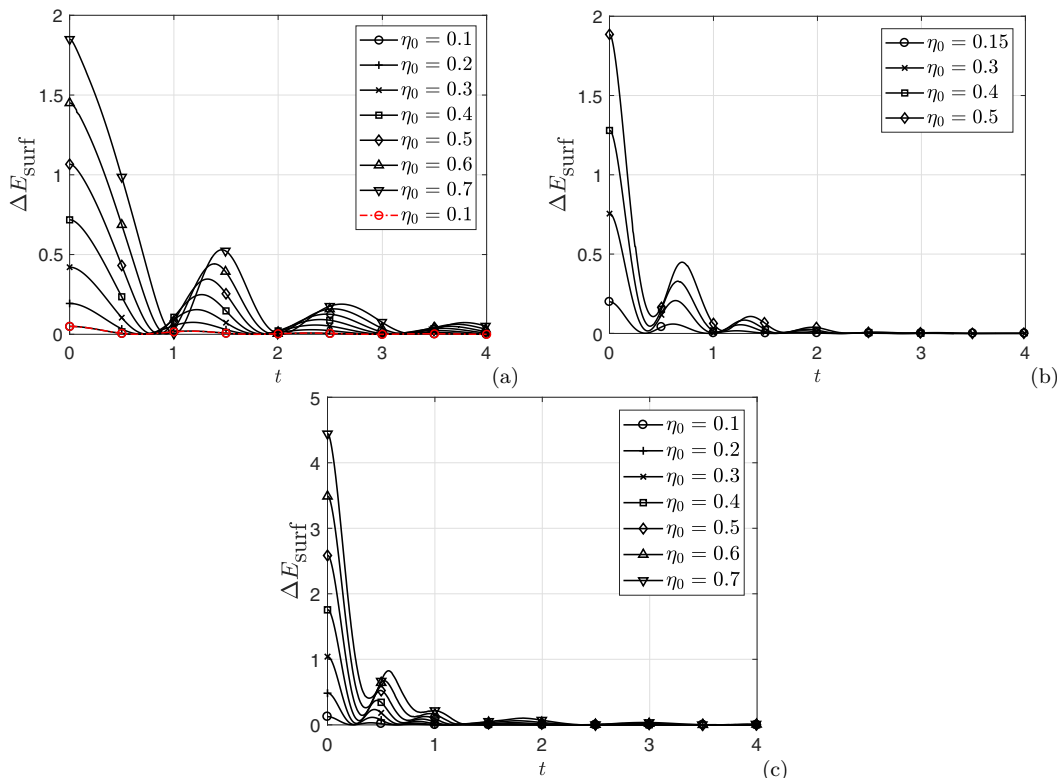
FIG. 22. Surface energy deviation from the spherical state $\Delta E_{\text{surf}} = \int_{\mathfrak{I}} 1 dA - 4\pi$ over time t for the different modes of initial deformation (a) $m = 2$, (b) $m = 3$, and (c) $m = 4$, with deformation parameters up to $\eta_0 = 0.7$ and Ohnesorge number $Oh = 0.1$. The red dash-dotted line indicates WNLT results.

VI. CONCLUSIONS

Axisymmetric shape oscillations of a Newtonian liquid drop in a dynamically inert ambient medium were studied. The oscillations were investigated using the analytical weakly nonlinear theory (WNLT) approach, and numerically with the extended discontinuous Galerkin (XDG) method. Oscillations start from a drop shape which is deformed against the spherical equilibrium state, with the deformation given by a Legendre polynomial of degree m. The number m counts the lobes of the drop shape in the direction of the polar angle of the spherical coordinate system. The deformation amplitude is determined by the value of a deformation parameter and varied between moderate and strong deformations. For the mode of initial deformation $m = 2$ and 4, the largest deformation parameter studied corresponds to a drop aspect ratio of 2.9.

Properties of the oscillating drops studied are the north pole position, the aspect ratio, as well as the kinetic, the surface, and the total energy contents of the drop as functions of time. The mode of initial deformation of the drop, the deformation amplitude, and the drop Ohnesorge number, as well as the initial velocity field inside the drop, are varied. The WNLT is a theoretical approach revealing the nonlinear properties of the oscillations. Since it is based on truncated series expansions of the field variables and the drop shape, however, it can be applied to moderate surface deformations only. Within this limit, the theory yields results in excellent agreement with the numerical simulations using the XDG method. This applies to both cases of the initially stagnant drop bulk and the velocity field as predicted by the WNLT. Oscillations starting from modes of initial deformation $m = 2$, 3, and 4, with deformation parameters η_0 up to 0.4, exhibit a damped oscillatory behavior of the drop
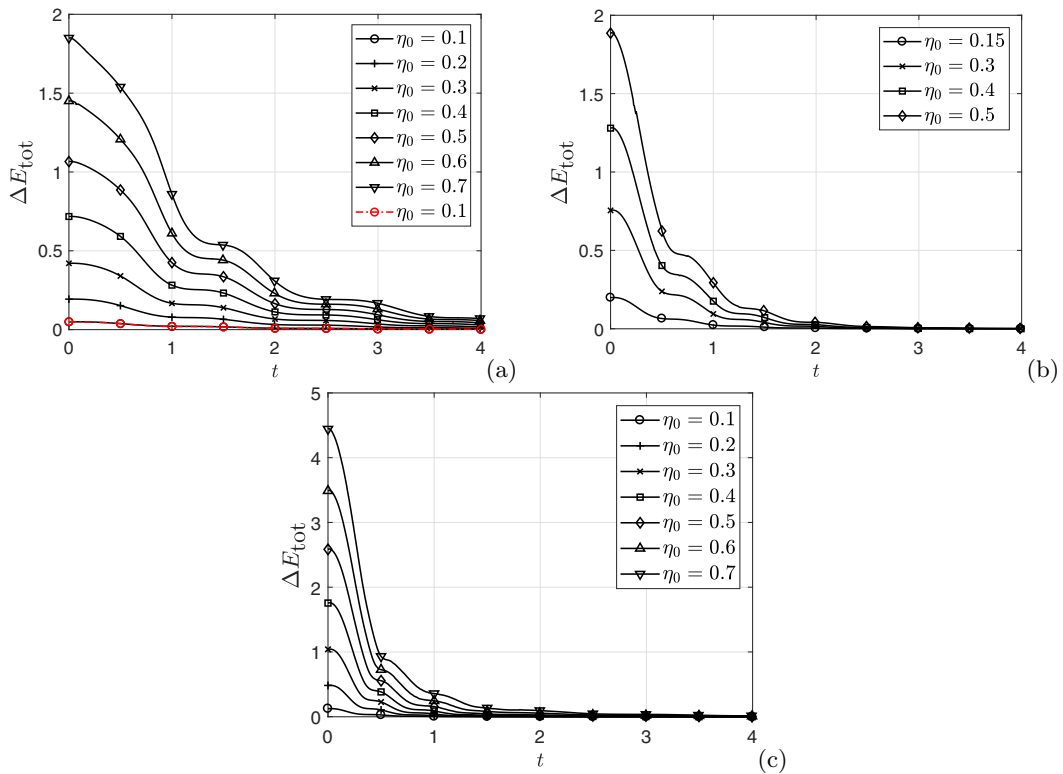
FIG. 23. Total energy deviation from the spherical state $\Delta E_{\text{tot}} = E_{\text{kin}} + \Delta E_{\text{surf}}$ over time t for the different modes of initial deformation (a) $m = 2$, (b) $m = 3$, and (c) $m = 4$, with deformation parameters up to $\eta_0 = 0.7$ and Ohnesorge number $Oh = 0.1$. The red dash-dotted line indicates WNLT results.

aspect ratio predicted equal by both methods and for both initially stagnant or moving drop bulk. The nonlinear behavior induces mode coupling, so that, in the evolution of the motion, modes different from the initial mode of deformation may be excited. For this reason, a drop with an Ohnesorge number of 0.56, which is predicted as supercritical by the linear theory when deformed according to $m = 4$, turns out to oscillate. The explanation comes from the excitation of mode $m = 2$, for which $Oh = 0.56$ is subcritical.

The Fourier power spectra of the presented data traces in time are studied and both the WNLT and the XDG method show nearly identical power spectra. Comparing the peak frequencies from the first oscillation period against the corresponding solution of the characteristic equation shows a decreased peak frequency for the first oscillation. This decrease is larger for higher modes of initial deformation and larger with increasing initial deformation parameter. Secondary peaks appear for mode coupling and as beats between the different oscillation mode frequencies.

The XDG simulations allow the energy content of the drop to be evaluated in a consistent manner, which is not possible with the WNLT. The analysis of the total (mechanical) energy content of the drop, composed from the kinetic and the surface energies, shows the expected dampening influence, with stronger dampening factors for the higher-order modes of deformation and the higher deformation amplitudes. At higher-order deformation modes $m \geqslant 3$ and moderate to large deformation amplitudes, the conversion of surface into kinetic energy and vice versa in time is not complete. The drop never reaches the spherical state until the dampening has strongly reduced the deformation amplitude.

The BoSSS source code is available under the Apache License at Ref. [42].

APPENDIX: DROPLET NORTH POLE POSITION OVER TIME

1. Comparison of the results from the XDG method and WNLT

In Fig. 24 we present the drop north pole position $r_s(0, t)$ as a function of time t for the three following cases with $Oh = 0.1$: $m = 2$ with $\eta_0 = 0.4$, $m = 3$ with $\eta_0 = 0.15$, and $m = 4$ with $\eta_0 = 0.1$. The evaluation of $r_s(0, t)$ for the XDG method is done by the summation of the droplet surface modes obtained by mode decomposition in terms of the spherical harmonics [see Eq. (38)]. The presented data traces in time are used for computing the Fourier power spectrum shown in Figs. 11–13 in Sec. V A 2.
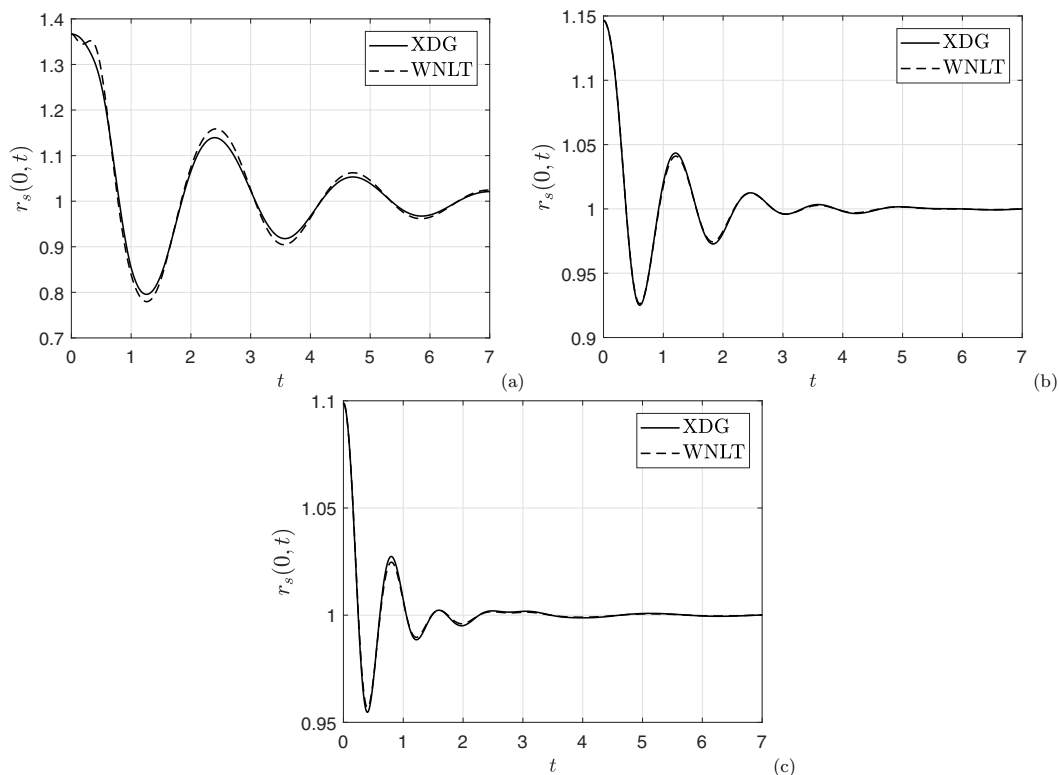

FIG. 24. Droplet north pole position $r_s(0, t)$ over time t for drops with $Oh = 0.1$—comparison of the WNLT predictions with the XDG results: (a) $m = 2$ with $\eta_0 = 0.4$, (b) $m = 3$ with $\eta_0 = 0.15$, and (c) $m = 4$ with $\eta_0 = 0.1$.
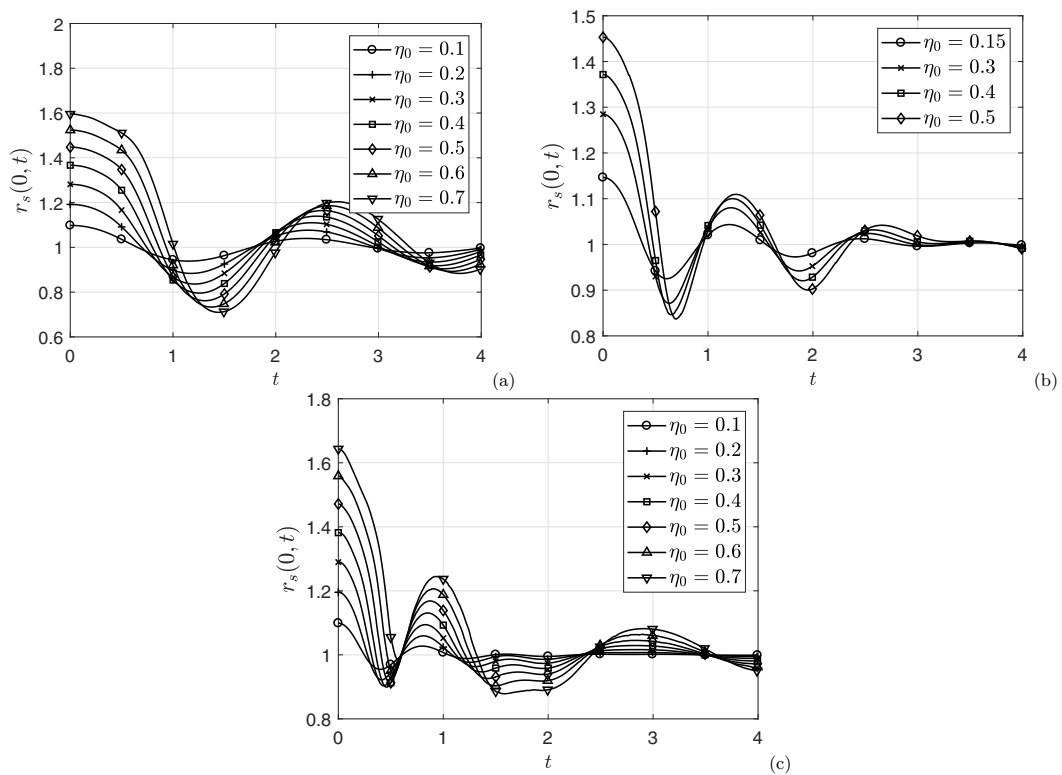
FIG. 25. Droplet north pole position $r_s(0, t)$ over time t for drops with $Oh = 0.1$ and different degrees of initial deformation in the modes of initial deformation (a) $m = 2$, (b) $m = 3$, and (c) $m = 4$. The deformation parameters up to $\eta_0 = 0.7$ are covered.

2. Large-amplitude study by the XDG method

In Fig. 25 we present the drop north pole position $r_s(0, t)$ as a function of time t for the three modes $m = \{2, 3, 4\}$ of initial deformation studied in this paper. The evaluation of $r_s(0, t)$ for the XDG method is done by the summation of the droplet surface modes obtained by mode decomposition in terms of the spherical harmonics [see Eq. (38)]. The presented data traces in time are used for computing the Fourier power spectrum shown in Figs. 18–20 in Sec. V B 2.

[1] J. W. Strutt, On the capillary phenomena of jets, Proc. R. Soc. London A **29**, 71 (1879).

[2] D. Zrnić and G. Brenn, Weakly nonlinear shape oscillations of inviscid drops, J. Fluid Mech. **923**, A9 (2021).

[3] D. Zrnić, P. Berglez, and G. Brenn, Weakly nonlinear shape oscillations of a Newtonian drop, Phys. Fluids **34**, 043103 (2022).

[4] G. B. Foote, A numerical method for studying liquid drop behaviour: Simple oscillation, J. Comput. Phys. **11**, 507 (1973).

[5] C. T. Alonso, The dynamics of colliding and oscillating drops, in *Proceedings of the International Colloquium on Drops and Bubbles*, edited by D. J. Collins, M. S. Plesset, and M. M. Saffren (Jet Propulsion Laboratory, Pasadena, CA, 1974).

[6] P. L. Marston and R. E. Apfel, Acoustically forced shape oscillations of hydrocarbon drops levitated in water, J. Colloid Interface Sci. **68**, 280 (1979).

[7] P. L. Marston and R. E. Apfel, Quadrupole resonance of drops driven by modulated acoustic radiation pressure—experimental properties, J. Acoust. Soc. Am. **67**, 27 (1980).

[8] E. H. Trinh and T. G. Wang, Large amplitude drop shape oscillations, in *Proceedings of the 2nd International Colloquium on Drops and Bubbles*, Vol. 82 (Jet Propulsion Laboratory, Pasadena, CA, 1982).

[9] O. A. Basaran, Nonlinear oscillations of viscous liquid drops, J. Fluid Mech. **241**, 169 (1992).

[10] O. A. Basaran, T. W. Patzek, J. R. E. Benner, and L. E. Scriven, Nonlinear oscillations and breakup of conducting, inviscid drops in an externally applied electric field, Ind. Eng. Chem. Res. **34**, 3454 (1995).

[11] B. Zhang, Y. Ling, P.-H. Tsai, A.-B. Wang, S. Popinet, and S. Zaleski, Short-term oscillation and falling dynamics for a water drop dripping in quiescent air, Phys. Rev. Fluids **4**, 123604 (2019).

[12] M. Agrawal, A. R. Premlata, M. K. Tripathi, B. Karri, and K. C. Sahu, Nonspherical liquid droplet falling in air, Phys. Rev. E **95**, 033111 (2017).

[13] M. Balla, M. Kumar Tripathi, and K. C. Sahu, Shape oscillations of a nonspherical water droplet, Phys. Rev. E **99**, 023107 (2019).

[14] M. Agrawal, R. K. Katiyar, B. Karri, and K. C. Sahu, Experimental investigation of a nonspherical water droplet falling in air, Phys. Fluids **32**, 112105 (2020).

[15] M. Perez, L. Salvo, M. Suéry, Y. Bréchet, and M. Papoular, Contactless viscosity measurement by oscillations of gas-levitated drops, Phys. Rev. E **61**, 2669 (2000).

[16] I. Egry, G. Lohöfer, I. Seyhan, S. Schneider, and B. Feuerbacher, Viscosity of the eutectic $Pd_{78}Cu_6Si_{16}$ measured by the oscillating drop technique in microgravity, Appl. Phys. Lett. **73**, 462 (1998).

[17] W. J. Hiller and T. A. Kowalewski, Surface tension measurements by the oscillating droplet method, PCH PhysicoChem. Hydrodyn. **11**, 103 (1989).

[18] C. Hsu and R. Apfel, A technique for measuring interfacial tension by quadrupole oscillation of drops, J. Colloid Interface Sci. **107**, 467 (1985).

[19] Y. Tian, R. Holt, and R. Apfel, Investigations of liquid surface rheology of surfactant solutions by droplet shape oscillations: Theory, Phys. Fluids **7**, 2938 (1995).

[20] R. E. Apfel, Y. Tian, J. Jankovsky, T. Shi, X. Chen, R. G. Holt, E. Trinh, A. Croonquist, K. C. Thornton, A. Sacco, Jr., C. Coleman, F. W. Leslie, and D. H. Matthiesen, Free oscillations and surfactant studies of superdeformed drops in microgravity, Phys. Rev. Lett. **78**, 1912 (1997).

[21] N. Aske, R. Orr, and J. Sjöblom, Dilatational elasticity moduli of water-crude oil interfaces using the oscillating pendant drop, J. Dispersion Sci. Technol. **23**, 809 (2002).

[22] X. G. Zhang, M. T. Harris, and O. A. Basaran, Measurement of dynamic surface tension by a growing drop technique, J. Colloid Interface Sci. **168**, 47 (1994).

[23] A. Ponce-Torres, J. M. Montanero, M. A. Herrada, E. J. Vega, and J. M. Vega, Influence of the surface viscosity on the breakup of a surfactant-laden drop, Phys. Rev. Lett. **118**, 024501 (2017).

[24] V. Kovalchuk, J. Krägel, E. Aksenenko, G. Loglio, and L. Liggieri, Oscillating bubble and drop techniques, in *Novel Methods to Study Interfacial Layers* (Elsevier, Amsterdam, 2001), pp. 485–516.

[25] F. Kummer, Extended discontinuous Galerkin methods for two-phase flows: The spatial discretization, Int. J. Numer. Methods Eng. **109**, 259 (2017).

[26] F. Heimann, C. Engwer, O. Ippisch, and P. Bastian, An unfitted interior penalty discontinuous Galerkin method for incompressible Navier-Stokes two-phase flow, Int. J. Numer. Methods Fluids **71**, 269 (2013).

[27] F. Kummer, J. Weber, and M. Smuda, BoSSS: A package for multigrid extended discontinuous Galerkin methods, Comput. Math. Appl. **81**, 237 (2021).

[28] M. Smuda and F. Kummer, On a marching level-set method for extended discontinuous Galerkin methods for incompressible two-phase flows: Application to two-dimensional settings, Int. J. Numer. Methods Eng. **123**, 197 (2022).

[29] F. Kummer, B. Müller, and T. Utz, Time integration for extended discontinuous Galerkin methods with moving domains, Int. J. Numer. Methods Eng. **113**, 767 (2018).

[30] R. I. Saye, High-order quadrature methods for implicitly defined surfaces and volumes in hyperrectangles, SIAM J. Sci. Comput. **37**, A993 (2015).

[31] M. Rieckmann, M. Smuda, P. Stephan, and F. Kummer, The extended discontinuous Galerkin method for two-phase flows with evaporation, J. Comput. Phys. **499**, 112716 (2024).

[32] T. Utz, F. Kummer, and M. Oberlack, Interface-preserving level-set reinitialization for DG-FEM, Int. J. Numer. Methods Fluids **84**, 183 (2017).

[33] P. R. Amestoy, I. S. Duff, J.-Y. L'Excellent, and J. Koster, A fully asynchronous multifrontal solver using distributed dynamic scheduling, SIAM J. Matrix Anal. Appl. **23**, 15 (2001).

[34] P. R. Amestoy, A. Guermouche, J.-Y. L'Excellent, and S. Pralet, Hybrid scheduling for the parallel solution of linear systems, Parallel Comput. **32**, 136 (2006).

[35] M.-C. Renoult, G. Brenn, G. Plohl, and I. Mutabazi, Weakly nonlinear instability of a Newtonian liquid jet, J. Fluid Mech. **856**, 169 (2018).

[36] E. Becker, W. J. Hiller, and T. A. Kowalewski, Experimental and theoretical investigation of large-amplitude oscillations of liquid droplets, J. Fluid Mech. **231**, 189 (1991).

[37] E. Becker, W. J. Hiller, and T. A. Kowalewski, Nonlinear dynamics of viscous droplets, J. Fluid Mech. **258**, 191 (1994).

[38] D. Gründing, M. Smuda, T. Antritter, M. Fricke, D. Rettenmaier, F. Kummer, P. Stephan, H. Marschall, and D. Bothe, A comparative study of transient capillary rise using direct numerical simulations, Appl. Math. Modell. **86**, 142 (2020).

[39] M. Smuda, F. Kummer, M. Oberlack, D. Zrnić, and G. Brenn, From weakly to strongly nonlinear viscous drop shape oscillations: An analytical and numerical study - plot data, 2024, doi:10.48328/tudalib-1425.

[40] J. A. Tsamopoulos and R. A. Brown, Nonlinear oscillations of inviscid drops and bubbles, J. Fluid Mech. **127**, 519 (1983).

[41] S. Meradji, T. P. Lyubimova, D. V. Lyubimov, and B. Roux, Numerical simulations of a liquid drop freely oscillating, Cryst. Res. Technol. **36**, 729 (2001).

[42] http://github.com/FDYdarmstadt/BoSSS.